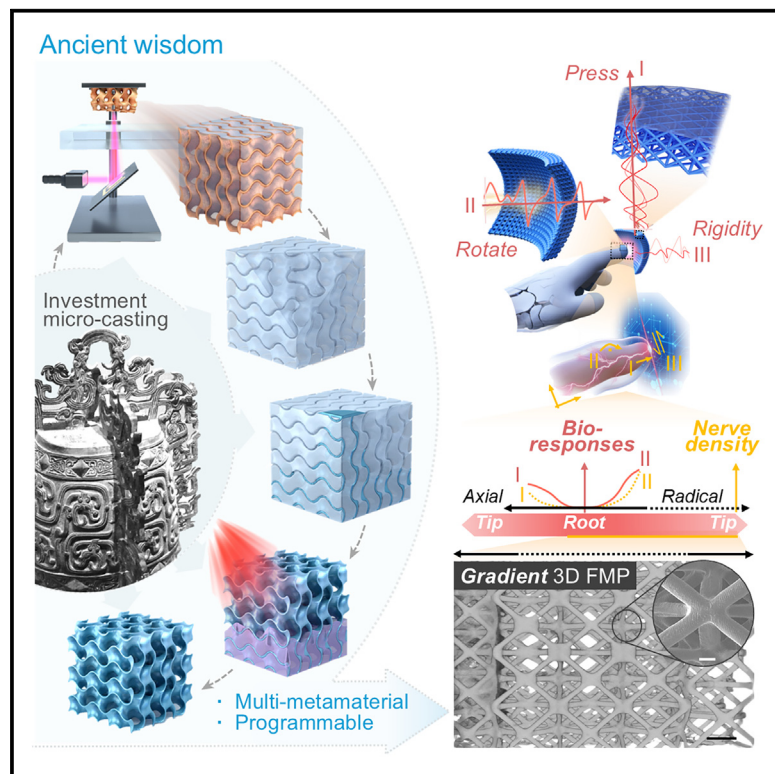


Investment micro-casting 3D-printed multi-metamaterial for programmable multimodal biomimetic electronics

Graphical abstract



Highlights

- Investment micro-casting 3D printing is proposed for programmable electronics
- Hydrophobic hollowed molds are formed via 3D soluble resin-based templates
- Over 20 types of challenging-to-form metamaterials are formed without destruction
- Biomimetic flexible piezoelectric devices are achieved for multimodal self-sensing

Authors

Chunjiang Wang, Xiaoming Chen,
Qihang Song, ..., Jie Zhang, Yang Lu,
Jinyou Shao

Correspondence

xiaomingchen@xjtu.edu.cn (X.C.),
jzhang12@xjtu.edu.cn (J.Z.)

In brief

Inspired by the ancient lost-wax casting made for engraved bronze, Wang et al. developed an investment micro-casting 3D printing strategy for the free assembly of more than 20 types of hard-to-form multi-metamaterials. A series of nerve-imitated flexible piezoelectric metamaterials are programmed for tailored properties and broadband responding. The comprehensive ability of integrated devices enhances the robotic biometric manipulation and stiffness perception in multimodal sensing and self-recognition.



Explore

Early prototypes with exciting performance
and new methodology

Wang et al., 2025, Device 3, 100658
May 16, 2025 © 2024 The Author(s). Published by
Elsevier Inc.
<https://doi.org/10.1016/j.device.2024.100658>



Article

Investment micro-casting 3D-printed multi-metamaterial for programmable multimodal biomimetic electronics

Chunjiang Wang,^{1,3} Xiaoming Chen,^{1,5,*} Qihang Song,¹ Jianxu Shi,³ Mengyong Lei,¹ Duo Ma,¹ Xiangming Li,¹ Xiaoliang Chen,¹ Hongmiao Tian,¹ Chunhui Wang,¹ Jie Zhang,^{2,*} Yang Lu,⁴ and Jinyou Shao¹

¹Micro- and Nano-technology Research Center, State Key Laboratory for Manufacturing Systems Engineering, Xi'an Jiaotong University, Xi'an, Shaanxi 710049, China

²Electronic Materials Research Laboratory, Key Laboratory of the Ministry of Education & International Center for Dielectric Research, School of Electronic Science and Engineering, Xi'an Jiaotong University, Xi'an, Shaanxi 710049, China

³School of Mechanical Engineering, Xi'an Jiaotong University, Xi'an, Shaanxi 710049, China

⁴Department of Mechanical Engineering, The University of Hong Kong, Hong Kong, SAR 999077, China

⁵Lead contact

*Correspondence: xiaomingchen@xjtu.edu.cn (X.C.), jzhang12@xjtu.edu.cn (J.Z.)

<https://doi.org/10.1016/j.device.2024.100658>

THE BIGGER PICTURE Introducing metamaterials into biometric electronics has been reported to enrich and innovate physical functionalities. Such performances rely heavily on the sophisticated combination of micro-units and higher-performing materials. However, forming compatibility among advanced materials and processing properties hinders the spatial shaping of multiple structures, composite selection, and function integration. To address this issue, we propose an ancient lost-wax-inspired approach, the Boolean-logic-guided investment micro-casting 3D stereolithography strategy (B μ SL), striking a trade-off in multi-metamaterial construction and alleviating the difficulty in function-oriented forming. The programmed piezoelectric multimodal neurological devices imitate delicate human manipulation with real-time grabbing feedback and stiffness self-recognition. It fosters the bridging of bio-like energy conversion with embodied intelligence, making no extra process limitation for biometric function integration.

SUMMARY

Biometric electronics have gained considerable attention in self-sensing, three-dimensional (3D) designs, mechanical drive, and multi-function integration. By leveraging these anisotropic capabilities into devices, metamaterial offers a promising pathway to exciting performance-oriented units. However, such distinctive mismatches in forming processes and inherent material properties are severely restricted in achieving cross-scaled microstructures, causing compatibility issues among well-defined bio-functions and fabrication. Herein, we propose an investment micro-casting 3D printing strategy for custom-molding multi-metamaterials without process barriers. This approach handles the bottlenecks of the hierarchical template replacement in ultra-hydrophobicity microchannels for the free assembly of more than 20 types of challenging-to-form materials. A series of piezoelectric metamaterials are programmed with broadband ranges, imitating nerve distribution that has human-feel touch, bending, and recognition. Our work benefits the stiffness self-perception in dynamic grabbing manipulation, broadening the application of multimodal electronics in bio-embodied robots.

INTRODUCTION

Biometric sensing electronics enable robotic hands to achieve dexterous manipulation and object recognition, such as softness, texture, and real-time feedback, in grasping tasks by mimicking the mechanoreceptors in human skin.^{1,2} These mechanisms are composed of three-dimensional (3D) microstructures in the shape

of wrinkles,³ protrusions,⁴ and villi for electrical signal transmission.⁵ 3D designs involving the layered,⁶ embedded,⁷ and arrayed functional material (FM) have emerged as prominent for multimodal bio-integration.⁸ Metamaterial, characterized by well-defined artificial structures and unprecedented performances,⁹ holds more potential to capture bio-like stimuli and bridge-function-oriented 3D mechanic designs.^{10–12} However, triggered by

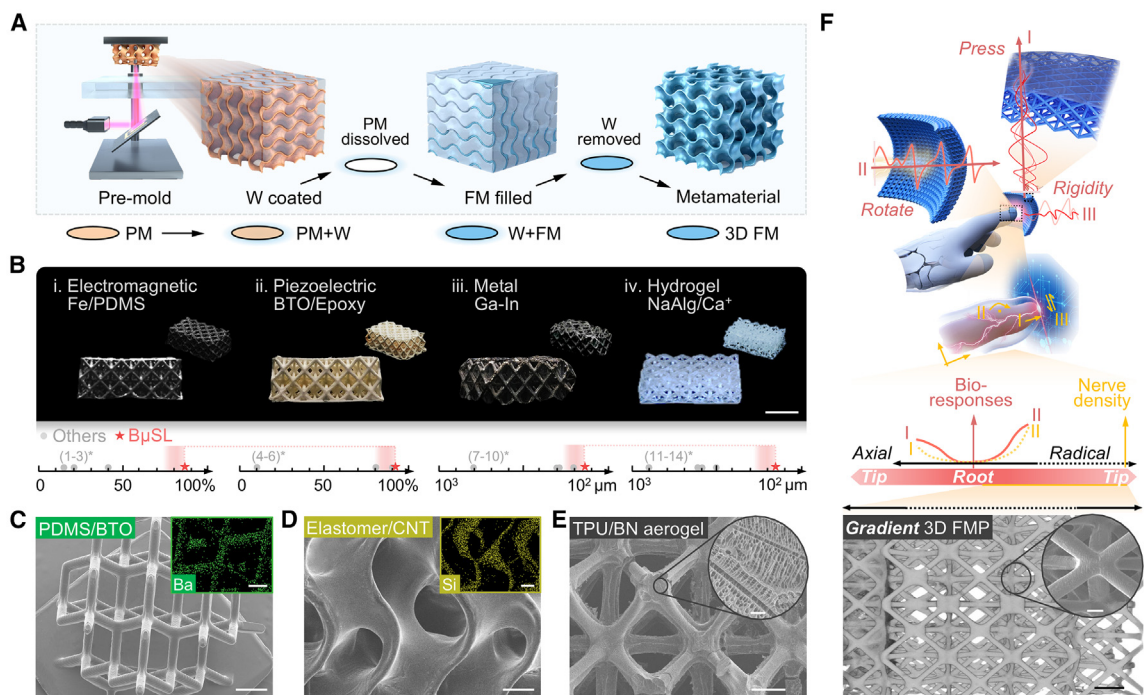


Figure 1. Boolean-logic-guided multi-metamaterial 3DP

(A) Schematic of the $B_{\mu}SL$ fabrication process via Boolean-logic-guided inversion.
 (B) Photographs of four typical hard-to-form FMs. Scale bar: 1 mm. The other methods referred to are described in Note S1.
 (C) SEM image of the 3D polydimethylsiloxane (PDMS)/barium titanate (BTO) FM. Inset: SEM-EDS mapping image, confirming the presence of Ba. Scale bars: 500 μ m.
 (D) SEM image of the 3D elastomer/CNT FM. Inset: SEM-EDS mapping of the Si distribution. Scale bars: 100 μ m.
 (E) SEM image of the 3D TPU/BNNS aerogel. Scale bar: 1 mm. Inset: SEM image of the regularly aligned pores with an average size of 3 μ m. Scale bar: 20 μ m.
 (F) Schematic of the biometric piezoelectric e-skin combined with its anisotropy function integration. SEM image of the gradient 3D FMP. Scale bar: 2 mm. Inset: SEM image of the single lattice. Scale bar: 200 μ m.

the broader 3D-unit expressions,¹³ the fabrication methods, including light etching,¹⁴ electrospinning,¹⁵ and transfer printing,¹⁶ have ignored FM versatility and spatial dimensions. This introduces mismatches in capability among composites and structures. In most cases, a single process has not matched multiple targets and their manifold properties.² Direct shaping challenges focus on FM-based hollowed bars,¹⁷ cross-scaled crystals,¹⁸ and cantilevers with high aspect ratios.¹⁴

As a common approach to integrating materials and structures simultaneously, 3D printing (3DP) has attracted significant interest in multiscale structure assembly.¹⁹ Property loss of FM occurs when component powders are subjected to laser,²⁰ thermal,²¹ and photonic irrigation.²² Modified interfaces and geometries may undergo material phase transitions on more minor scales. Dispersion patterns of ink uniformity, fluid shear thinning, and powder re-aggregation are keys to complete printing.²³ It is critical to minimize as much as possible the adverse printing effects in extreme process operations for various characteristics of FM.

Nowadays, template-mediated demolding methods have been established to mitigate reliance on FMs. The ablation,²¹ encapsulation,²⁴ and dissolution of 3D molds could avoid harmful energy field contact on FM surfaces.²⁵ But then again, the heterogeneous shape-controlled templates and internal residues are hard to remove while being exposed to high tempera-

tures and pressure. Shape definitions of diverse templates are not consistent in a stationary avenue.²³ Moreover, functional loadings, partial contenting, and matrix rheology restrict poor repeatability and structural resolution. This may bring about more difficulties in cross-scale formation. As a stricter prerequisite, the removal processes among FMs and templates were inevitably challenged; for instance, organic immersion and acid etching should be isolated to avoid a reaction with the FM for phase separation.^{26,27} This adds another barrier to the selection of suitable multiple metamaterials. Devices always prefer to contain more functional phase content dispersed in various polar solvents, which weakens the template casting in indirect molding. Therefore, if 3DP is redefined via template free printing, no-residual removal, full injection, and demolding, then a universal scheme would be developed to encompass the compatibility of multiple metamaterials with as little process intervention as possible.

In this article, inspired by the ancient lost-wax casting made for engraved bronze, we propose a new approach, Boolean-logic-guided investment micro-casting 3D stereolithography, denoted as $B_{\mu}SL$ (Figure 1A). The approach includes a two-step precise template replacement (Video S1). A defined pre-mold (PM) with complex structures was prepared for the continuous 3DP of soluble resin, and the melted wax was

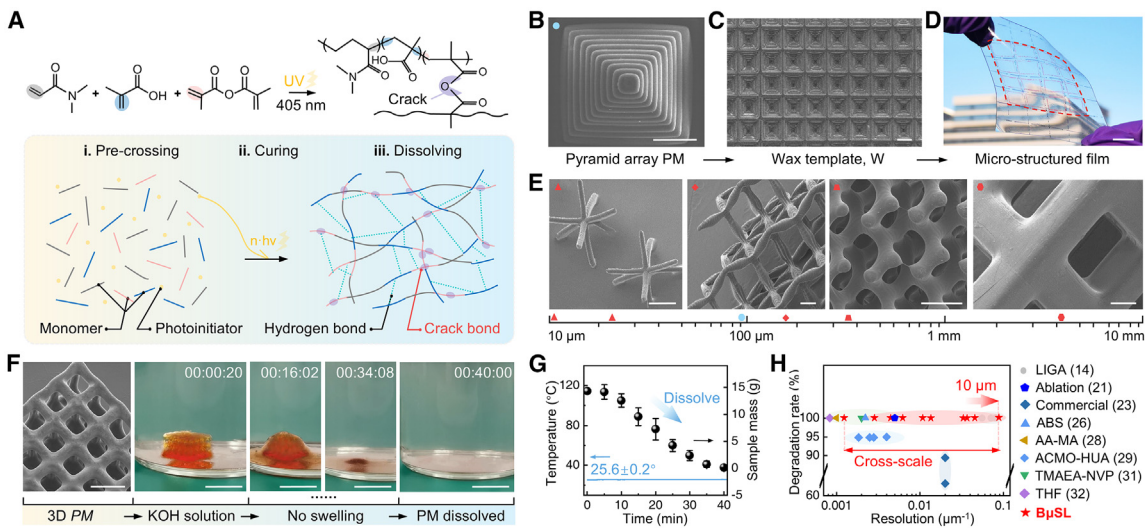


Figure 2. Cross-scaled 2D and 3D soluble templates

- (A) Diagram illustrating the mechanism of the organic photosensitization reaction based on UV light and crosslinking to form covalent, hydrogen, and crack bonds.
 (B) SEM images of a micro-pyramid-array PM. Scale bar: 200 μm.
 (C) SEM images of a wax template. Scale bar: 1 mm.
 (D) Photograph of a stretched 2.5D PDMS film.
 (E) SEM images of the 3D PM exhibiting cross-scale feature dimension from 10 μm to 4.1 mm.
 (F) SEM image of a sample to be dissolved. Scale bar: 1 mm. Experimental snapshots of the sample during dissolution. Scale bar: 1 cm.
 (G) Changes in the mass of PM and the real-time temperature with a complete dissolution period.
 (H) Comparison of the degradation rate and feature resolution obtained by BµSL with eight typical structure-removing printing methods.

employed as a removable mold. Then, the hollowed mold (W) was infiltrated for the clear wax washing out via electrowetting (the first inversion). The FM composed of pre-treated nanocomposites was printed (the second inversion) after forced infusion and solidification, whether on a macro- or microscale, which would cover more than 20 types of material selections (Figure S1). Two typical FMs were printed with electromagnetic and high-absorptivity nanoceramics with unusual contents. The others were hard-to-print 3D In-Sn metal and hydrogel (Figure 1B). Two types of FMs with constructed micro-trusses were printed for complexity validation (Figures 1C and 1D). In addition, a hierarchical 3D aerogel was promoted with other modifications like freeze drying (Figures 1E and S7). Due to the ability for free assembly, a biomimetic piezoelectric 3D FM e-skin (FMP) was employed and parameterized to transmit the press, rotate, and rigidity actions in real time (Figure 1F). BµSL realized the gradient micro-unit array to be packaged in robotic manipulation for a reinforced learning system. It showed multiple bio-functions involving a wide range of pre-ceived responses and multimodal self-recognition. Our approach would simplify the forming complexity of multiple metamaterials and unlock abundant bio-applications.

RESULTS

Cross-scaled 3D soluble template

Reasonable control of the exposure resolution of soluble resin is key for achieving continuous, precise 3DP for PMs. As a basic practice, we synthesized an ultraviolet (UV) resin that achieved

rapid crosslinking with high resolution and complete degradation without swelling. The combination of the acrylic groups can induce a decomposition reaction through the pre-polymerization of acrylic acid (AA) and acrylamide (DMA), together with the copolymerization with anhydride (MAA), in ambient conditions (Figure 2A-i). The association of the crosslinker with photons triggers an energy release, initiating addition reactions that give rise to tightly connected networks through the formation of hydrogen and covalent bonds (Figures 2A-ii and 2A-iii).²⁸ Subsequently, the moieties of the MAA chains in cured resin fluently dissolved into an -AA-DMA- salt solution undergoing neutralization and degradation.

To obtain the relative maximum light-induced vitality of resin, we adjusted the sensitivity peak to 401 ± 20 nm. Then, the tolerance of the curing depth per unit was enhanced by adding UV absorbers. Each layer of projection could be precisely tailored to link various exposure energies with different curing depths, expressed as a regular logarithmic linear relationship (Figure S2). A pre-treatment was added for the rapid continuous 3DP of monomers (see methods), making it applicable to the projections of any PM design. Figures 2B and 2C show the PM of the micro-structured pyramid array creation based on the demolding of resin, which could form a large-scale structural polydimethylsiloxane (PDMS) film (Figures 2D, S3A, and S3B). In addition, the printing process can be employed to form various cross-scaled 3D latticed PMs with a critical dimension ranging from near 10 μm on the microscale to 4 mm on the macroscale (Figures 2E and S3C–S3F). When a cubic-scaffold PM was subjected to an alkaline solution, it rapidly underwent complete

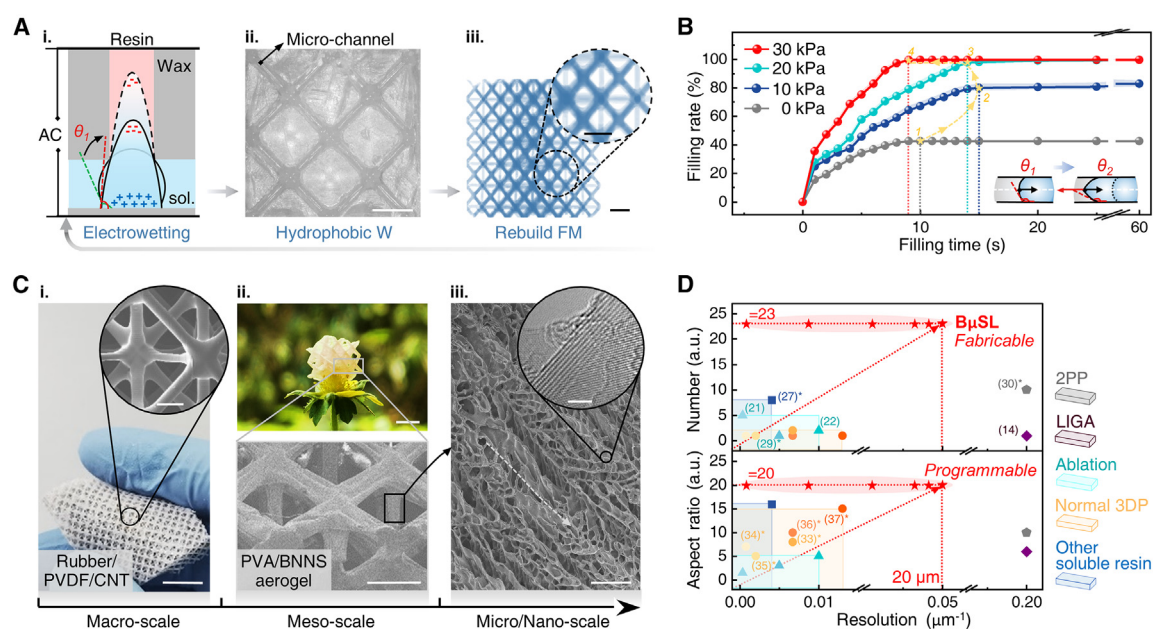


Figure 3. Forming of cross-scaled 3D FMs

(A) Schematic diagram of PM removal processes from the micropores. (i) shows the schematic diagram of the electrowetting process. (ii) is the optical image of the superhydrophobic hollowed W. Scale bar: 500 μ m. (iii) shows the reverse image of the 3D microchannels obtained via μ -CT. Scale bars: 500 μ m.

(B) Influence of the filling time on the filling ratio for different pressures.

(C) Cross-scale 3D FM. (i) is the photograph of a 3D nanocomposite-reinforced FM. Scale bar: 1 cm. Inset: SEM image of the micro-truss. Scale bar: 500 μ m. (ii) is the photograph and SEM image of a 3D aerogel FM. Scale bars: 5 mm (top) and 1 mm (bottom). (iii) shows the enlarged SEM image of a selected branch with aligned micropores. Scale bar: 10 μ m. Inset: Transmission electron microscopy (TEM) image showing the ladder effect of BNNS. Scale bar: 10 nm.

(D) Comparison of the other 3DP methods.

hydrolysis without swelling (Figure 2F; Video S2), and the temperature fluctuated within 2°C for 40 min (Figure 2G).

In contrast to others, the minimum feature dimension of the structured PM is about 22 μ m, far outpaced by the other template removal methods (Figure 2H). Even though the minimum feature resolution of lithography, electroplating, and molding (LIGA) could be extremely high, B_μSL still has advantages in the 3D shaping and rapid degradation of cured resin, whose function is like that of a photoresist. Besides, our developed soluble resin could surmount the restriction that smaller digital projection units required to surpass the sub-microscale to approximately 10 μ m (Figure S4). Moreover, the dissolved rate, as one of the most significant indicators of whether a sample is completely dissolved in the solution without solid residues, will become the key to micropore replacement. Methacrylate is completely soluble in water, and the rate could reach 100%, which is hardly achieved for the reported constituent organic groups, such as acrylonitrile butadiene styrene (ABS),²⁶ 4-acryloylmorpholine (ACMO),²⁹ and others (details in Video S2; Table S1).^{30–32}

Free assembly and regulation of 3D FM

Most of the traditional indirect 3DP strategies only have one-step substitution, increasing the presence of unacceptable microstructures, like dead zones, no support rods, thin walls, and collapsible shells. Though demolding twice avoids these issues, it brings the bottlenecks of PM removal and FM filling. B_μSL exhibits the exchange and extraction of a soluble PM

hidden inside the deep crosslinked microcavities. Efforts should be aimed at the ultra-hydrophobic inner wall determined by wax. The negative pressure effect leads to persistent underfilling due to the trapped air, thus resulting in an incomplete infiltration status among liquids and solids (Figures S5A and S5B). Upon analyzing the droplet wetting behavior (Figure 3A-i), the contact angle θ_v , which exceeds 90°, can be reduced by applying a spatial electric field (E_a) on both sides of the W (details in the methods). The reason is that the even charge distribution due to the electric field modifies the total internal energy (F_a), leading to changes in the droplet shape. Then, it allows the solution to flow into the ultra-deep microcavities.

In order to ensure full dissolution, the electric field vector fluctuated to enable the residual PM to be repeatedly washed and displaced by the flowing solution (Video S3). θ_v changes in solution flow were measured entirely linearly with the electric voltage from 0 to 15 kV, as well as considering that wetting co-occurs in various regions of W. Here, finite element analysis (FEA) was performed to quantify the effectiveness of electrowetting in inducing ultra-hydrophobic conditions. Each deep hole with diverse shape parameters was fully wetted (Figures S5C–S5E). In practice, we employed the diverse W with residual PM parts for the wetting (Figure 3A-ii). As anticipated, the liquid inside the channel could infiltrate into the deep hole and the dissolving resin polymer, while the fresh solution outside can be replaced in real time, especially in the interlaced microtube with a large

aspect ratio of 20 and a minimum feature of approximately 50 μm . As reconstructed through microcomputed tomography ($\mu\text{-CT}$), the inner channels were confirmed to be smooth without any detectable contamination (Figure 3A-iii).

As for the reverse infiltration process of PM removal in microtubes, various FMs should also be completely moistened and smoothly filled in W. However, most FMs hardly display any polarization resistance and maintain unstable dielectric properties in electro-assisted fields. In analytical expression, melted or liquid FMs must overcome the resistance force (F_{in}) to fill the spatial microscales, considering an ideal micropore scenario (see methods). Not all the air could be expelled from microchannels, resulting in localized cavities and discontinuous 3D FM. We propose an FM-filtrated filling approach within constant hydraulic pressure, and more air is discharged along the top-to-bottom path (Figure S6A). It is foreseeable that the filling process is grueling until the outer pressure is set up to 30 kPa, regardless of the void proportion of the channel pre-made from 0 to 30 (Figure S6B). For instance, the polyurethane matrix with a dynamic viscosity of 181 Pa s could be filled into an octagonal-truss-templated W (minimum feature to 50 μm) in merely 7.6 s within 30 kPa (Figure 3B). The differential pressures driving air expulsion maintain a static force suitable for each conduit. The saturation filling processes closely match the theoretical curve after surpassing a critical pressure of about 10 kPa. Additionally, the needed filling experiences in Figure S6C show an increased trend of pressure along the air-expelling direction aimed at enhancing the filling ranges. Eventually, an arbitrarily defined large-scale (around 4 cm^3 cubic sizes with a dimension of 100 μm), hollowed W was achieved without obvious geometric defects (Figure S6D).

The fabricable stability of $B\mu\text{SL}$ makes it suitable for constructing multiple FMs. The complexity of the metamaterial did not need to be considered; $B\mu\text{SL}$ showed an unparalleled superiority in cross-scaled printing. At the macroscale, a 3D rubber-based PVDF/carbon nanotube (CNT) microscale polycrystal lattice was printed with a 100 μm minimum feature resolution (Figure 3C-i). To show the structural controllable capability at the microscale, an ultralight polyvinyl alcohol/boron nitride nanosheet (PVA/BNNS) 3D aerogel was formed with hierarchical features (Figure 3C-ii). Besides, the external physical fields can be aided to manipulate the particle states in $B\mu\text{SL}$. These are supposed to align in orientation, nanocomposite solidification, micromorphology control in film surfaces, and stratified deposition in design (Figures 1F and 3C-iii). $B\mu\text{SL}$ has the potential for *in situ* deposition of district FM through block-like building as well the need for an involved FM aerogel and an available matrix for the local or overall function enhancement (Figure S7). To conclude, five clarified groups were compared in Table S2, and the superiority over the other methods is pointed out in Figures 3D and S8. $B\mu\text{SL}$ profited greatly from free-assembling FMs without the need for harsh reaction conditions or sacrificing the capability of macroscale shaping. In sum, our strategy reduced the restriction of free combination and expanded the diversity of FMs (Table S3). $B\mu\text{SL}$ could achieve a minimum size of 20 μm and an aspect ratio of around 20; furthermore, over 20 types of FMs were utilized through Boolean-logic-medicated demolding.

Neuron bio-driven programmable 3D e-skin

Motivated by the superiority of $B\mu\text{SL}$, our exploration delved into a programmable creation mode of e-skin. Human skin relies on the transmission of electrical signals originating from tactile and vibratory neurons to perceive external stimuli.^{1,4} Most neurons in the cross-section of human finger skin are in the epidermis, also distributed at the axial tips that set more than radical tip areas (Figure 4A).³³ The imitated gradient structures of molding sandwiched,⁴ gradient,³⁴ mold casting,³⁵ and metatlattices³⁶ heavily rely on direct extrusion printing of molten FMs, thus confining them into macroscopic incompatible trusses. It takes a long time to couple mechanical and piezoelectric responses, either in bionic devices or similar metamaterials. We crafted a mechanics-driven design and showcased unique self-responses in pressure responding via 3D piezoelectrical devices (Figure S9A). Then, the latticed FMP could be engineered consisting of various rods (abstracted as a vector, L) to adjust the mechanical properties, which were arranged by the octagonal parametric design, denoted as FMP_x ($x = 1, 2, \text{ or } 3$) (Figure S9B). The stiffness increases along the central axis, leading to a higher density of the sensory lattices. FMP_x reacted with the stress matrix (σ), followed by electric displacement (D) in each rod and generated piezoelectric charges (V) along each lattice principal stress direction. The effective piezoelectric voltage constant, $d_{3n} = \sum \int v D_{nk} dV_i / \sum \int v \sigma_{ki} dV_i$, was transformed into d_{nk} through the Cartesian coordinate matrix, N_i , to gain the volume integral of the voltages (see derivations in methods).

Variations in the distinct direction of FM rods induce changes in the response matrix. Hence, designs incorporating different structural densities (ρ_x) would result in a set of structure families characterized by unique effective d_{3nx} regardless of the selected FM. We conducted a three-phase physical simulation on the strain and piezoelectric responses of FMPs (Figures S9C and S9D). FMP_1 , as the lower-density device, exhibited an obvious deformation and higher integral stress in a lower load, thus leading to a more substantial voltage compared to FMP_3 . However, there is an inflection point, and 3D interconnected rods reached the compression limit, causing the transformation matrix, N_i , to be equal to 1 (see methods). FMP_3 responded to generating greater D_n and V in heavy loads with its high density, showing the possible program of the outputs. We fabricated FMP_x and a discontinuous gradient-arrayed lattice FMP, referred to as FMG, composed with a PVDF/BNNS/CNT-reinforced rubber composite, and showed the even presence of the B and N elements (Figures S10A-S10D). The $\mu\text{-CT}$ imaging reconstruction of FMG reveals that the overall structural defect concentration is below 3.8% (Figure 4B). Then, we formed FMP_x with three design parameters in a common lattice unit (Figure 4C). *In situ* scanning electron microscopy (SEM) imaging shows that the obtained rods are intact without obvious structural fractures (Figure 4D). In addition, FMG could withstand bending activity without the appearance of wrinkles on the microscale (Figure 4E). Impact tests revealed that the fracture strength of FMG was less than 6.9 MPa, which exhibited greater impact resistance than that of FMP_1 and FMP_2 (Figures S10E-S10F). FEA was conducted, and it was found that FMP_x with low density could withstand

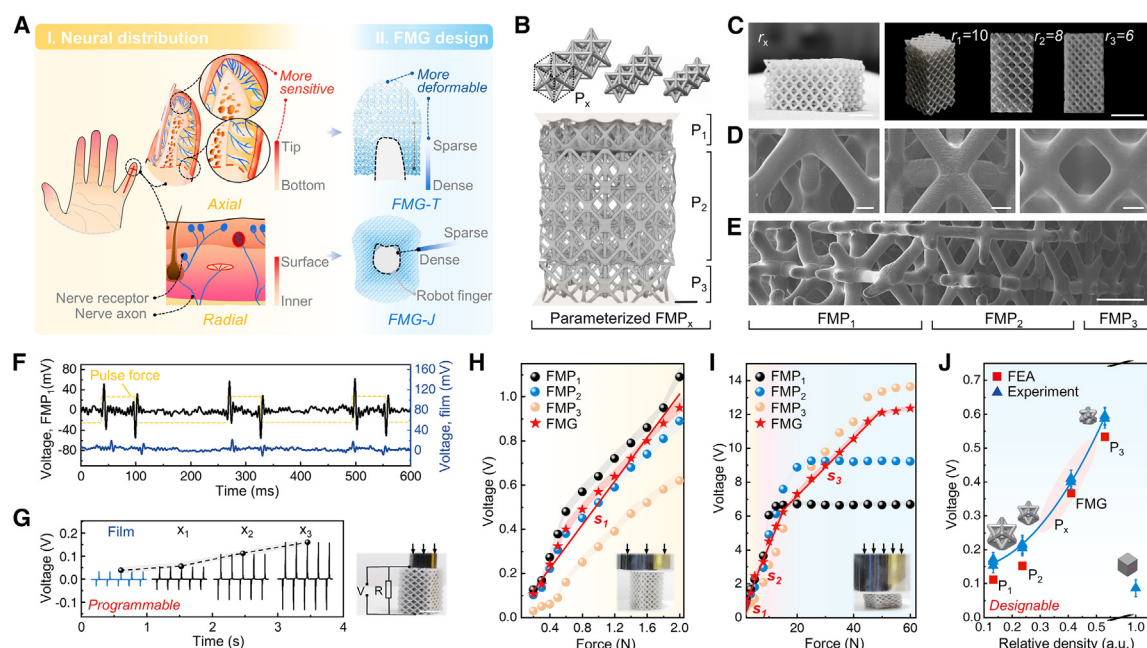


Figure 4. Biological-sensing-inspired 3D FMP with tunable programmability

- (A) Schematic of the biological design (II) inspired by the subcutaneous nerve distribution (I) in the human finger.
- (B) Parameterized FMP_x with typical lattice constants, namely $r_1 = 10$, $r_2 = 8$, and $r_3 = 6$ (top). μ-CT reverse scanning image of a 3D FMG (bottom). Scale bar: 2 mm.
- (C) Photograph of FMP_x. Scale bar: 1 cm.
- (D) SEM images of FMP_x, and images from left to right are P₁, P₂, and P₃ in order. Scale bars: 200 μm.
- (E) SEM image of bent 3D FMG. Scale bar: 2 mm.
- (F) Voltage outputs as a function of time for FMP₁ and 2D film device under 1 kPa impact force.
- (G) Piezoelectric responses of FMP_x at 1 kPa. Inset: photograph of the FMP₁ testing circuit. Scale bar: 5 mm.
- (H and I) Peak-to-peak voltages responded from the weak and heavy impact forces of FMG. s_1 , s_2 , and s_3 are linear fitting curves that represent sensitivity in the three impacting ranges, respectively.
- (J) Experimental and FEA simulation results regarding the structural relative density and voltage output.

the initial deformation, while the high-density devices could respond in a relatively heavy impulse loading.

In the experiments, FMP_x and FMG were encapsulated inside flexible electrodes to generate a piezoelectric effect for corona polarization. FMP₁ showed a peak-to-peak output sensitivity that is 20 times greater than that of the 2D piezoelectric films under a 1 kPa pulse (Figure 4F; Video S4). FMP₁ exhibited a positive correlation between the electrical response and positive force with a maximum delay of 6.7 ms and a linear force-electrical coupling of 27.4 V/MPa (Figure 4G). Except for FMP₃, sensitivities not less than 30 V/MPa were observed within a load range of 0.8–8 kPa. The stability was maintained over 4,000 pressure cycles, with a step response and no variations observed (Figure S11). Under the force range of 8–300 kPa, FMP₁ and FMP₂ show anti-compression characteristics, reaching output saturations at 34 and 71 kPa, respectively (Figures 4H and 4I). Conversely, FMP₃ and FMG showed stable signals at a higher level at 240 kPa. FMG was uniquely activated and generated a stable charge, and its gradient structure could be expected to achieve the addressed and wide-ranged outputs by variable loading responses. The step linear sensitivity was marked as slopes s_1 and s_2 in the lower pressure range and s_3 with a rela-

tively gentle slope. In the end, the relationship between the relative density and the peak-to-peak output can be preserved as a corresponding non-linear fit (Figure 4J). The differences deviated to an average value of less than 7.2% by FEA results.

Indifference grasping and multimodal recognition

By programming 3D FMG lattices, it becomes feasible to estimate potential changes in specific situations, enabling the generation of signal feedback in time. Most cases regarding the tactile perception of robot appendages, such as softness and roughness, have involved hybrid responding and multimodal sensing.³⁷ Our developed wide-ranged and self-powered 3D e-skin has made it significantly easier to achieve compound perception. Herein, by employing the position-addressable FMG at the fingertips (FMT) and joints (FMJ), a bionic-array sensing system (BASS) was realized through *in situ* motor activation and deactivation (Figure 5A). Under the pulse load impact, FMT responded to a stepwise linear progression. The variation of the electrical-force response fit was less than 1.4% within a less-cycle range, and the fluctuations did not exceed 0.7% in ranges of 10^4 cycles (Figures S12A–S12C). This good stability may be attributed to the good performance of

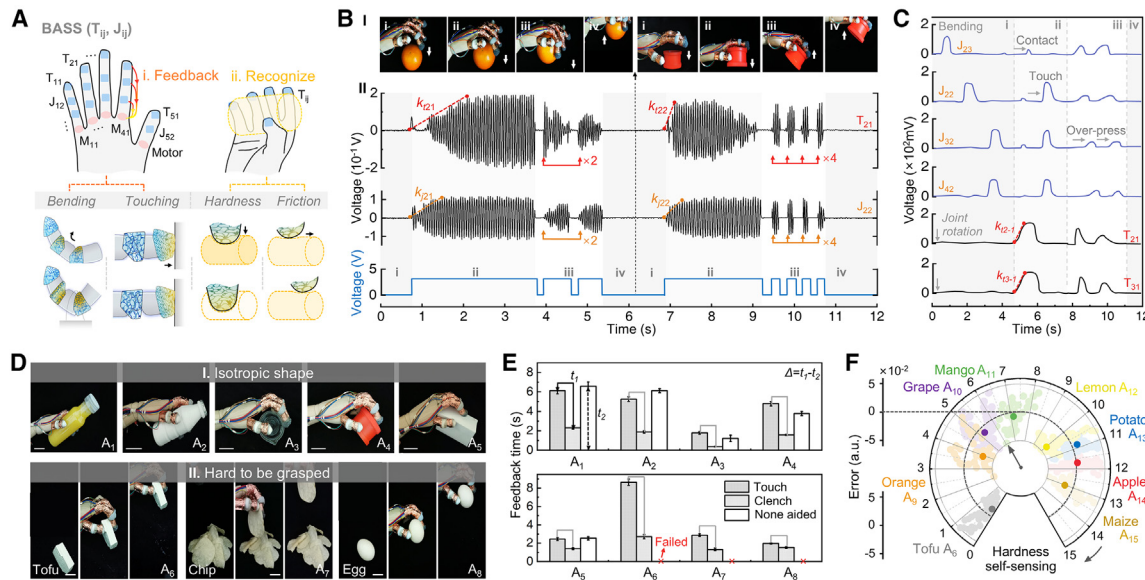


Figure 5. Self-powered multimodal BASS

- (A) Schematic of the BASS for grasping and recognition.
- (B) BASS-enhanced manipulators utilized for grabbing an object. (I) is the experimental snapshot of grasping an orange and a box. (II) shows the real-time voltage responses together with motor rotation.
- (C) Envelope voltage curves as a function of time during four typical stages.
- (D) Photographs of the grasping of objects with isotropic-shaped objects (A_1 – A_5) as (I) and hard-to-grasp objects (A_6 – A_8) as (II). Scale bar: 1 cm.
- (E) Comparison of the clamping times in status of three different grippers. t_1 is the addition of touch and clench time, and t_2 is the comparison bracket of no BASS-aided grasping.
- (F) Polar-coordinate diagram of the stiffness estimated by experiments and standard values. The numerical value of radial coordinates represents the deviations of the second decimal point in the raw data of tested hardness.

the nanofiller-enhanced rubber matrix. FMJ was linked to joint flexion angles and controlled by servo motor pulses (Figures S12D–S12F). Delightfully, the bio-functions were fully showcased in the hidden features of signals. Due to the flexibility of FMT, its deformation was proportional to the interfacial friction, with the slopes of the peak envelope being related to stiffness (Figure S13). Thus, the micro-protrusions of the object surface induced FMT to generate a stepped and identifiable output by stable sliding. Despite the force sensitivity responding ability of FMJ, stable outputs also indicated the loading ability in the bent situation.

Non-destructive, delay-free, and uniform grasping has been a continuous challenge for manipulators that lacked feedback. Herein, an orange and a box were each grasped to assess the BASS modes, followed with each robot finger (Figure 5B-I). The typical grasping process is divided into four stages: pre-contact, contact, overload compression, and lifting (Figure 5B-II). Upon initiation, FMJ₂₁ (simplified to J_{ij}, where i and j are equal to 1 and 5) responded to the motor rotation and could detect the joint flexion angles. Subsequently, when in contact with the surface, FMT₂₁ (T_{ij}) deformed during stiffness sensing and generated the signal slope, k₂₁. As the maximum initial torque began, neither T₂₁ nor J₂₁ registered any responses. Following this, the motor secured the finger firmly for clamping until none of the devices had any outputs, and the judgment logic process is shown in Figure S14. The orange sample was fully grasped after two iterations. Four iterations were necessary for the box to be

grasped (Video S5). Any touching signal features from FMT/J were allowed for validation in real time via independent data extraction in BASS (Figure 5C). The envelope of output here was the first-order fit curve from the highest responding voltage converted from each vibration. To obtain the stiffness values of grasping objects more precisely, we extracted time domain responses matrixes (K) in different locations and used them as input for the prediction model (Note S6). We employed a reinforcement learning strategy to capture the slope, k_{ij}, of multiple object grasps, relying on an analyzed database from T_{ij}. In the 40 cycles of pre-training grasping, we recorded changes in the signal envelopes experienced by the agent (s) to form a long-term-accumulated expected reward (Q). The K matrix continuously interacted with the standard stiffness values (S) obtained by the instrument, observed the reward (r), and transitioned to the next state (s') until Q was converged.

Through such learning for various stiffness values (from 0 to 1.5×10^6 Pa), the perception results were reinforced, reducing the stiffness error to 1.46%. BASS could pinch A₁–A₅ irregular objects and A₆–A₈ hard-to-grasp objects (Figure 5D). Comparative results reveal that BASS is capable of discerning when and whether to clamp, effectively replicating the nerve signal feedback of the human hand (Figure 5E). Compared with the non-BASS-aided robot hand, which failed in grabbing tofu, chips, and an egg, the sum of the actuation times of touch and clench phases was higher than the hard contact process. It provided enough friction and time for deformable objects to be picked

up without damage ([Video S6](#)). Coinciding with this, when grabbing fruits of various stiffnesses from A₉ to A₁₅, the prediction values deviated by less than 2.74% compared with the standard stiffness values gained from instruments. Similarly, the recognition results showed similar prediction trends and controllable errors while grabbing the other objects A₁–A₈ ([Figures 5F](#) and [S15](#)). The outstanding integrated functions of BASS, assisted as a bio-hand with rapid feedback, multimodal decoding in grasping, and recognition, as well as the comprehensive performance of bio-inspired electronics, are presented in detail in [Figure S16](#) and [Table S4](#). Our approach compensates for the conflict between the rigidity and sensitivity of devices, even gathering self-powered systems. FMG/FMJ would possibly be crafted in a suitable conformal shape in the embodied intelligent robot finger. It not only validates the use of the BμSL for engineering biomimetic piezoelectrical devices but opens a new possibility for free assembly with unrestricted 3D design.

DISCUSSION

This strategy, BμSL, is proposed for shaping the challenging FM through free structural design and free assembly of composites. In contrast to the conventional methods, BμSL overcomes the process constraints for small ranges of FMs in extreme conditions to achieve multiscale (from 20 μm to 4 mm), high-aspect-ratio (up to 20), and multiple kinds of (>20) FMs with complex geometric features. Our approach is certainly not limited to thermosetting composites, and it can be applied to metals, aerogels, hydrogels, and nanocomposite-reinforced FMs. Notably, the soluble resin offers an innovative route in rapid 3D prototyping as an alternative to 3D photoresists. BμSL enables the presence of more extensive physical interactions in multilayer microarchitectures. Due to its benefits, applying *in situ* multi-material deposition is another option for more possible material combinations. It can be extended but is not limited to thermal, mechanical, and electromagnetic performance, as it will be coupled with an adjustable property in each scale.

Triggering new possibilities for self-powered electronics, BμSL presents a new paradigm for 3D biomimetic metamaterials. It shows a wide response range of 8–240 kPa and a high sensitivity of near 30 V/MPa for FMP_x with deformable and gradient responses. With a multimodal integrated perception capability, BASS could provide a database to perceive stiffness and enhance grasping ability via reinforcement training. FMP_x via direct design driven without barriers was employed for flexible tentacles, soft grabbing, and smart recognition. The piezoelectrical 3D e-skin that delivers dynamic feedback highlights its good programmability as multimodal metamaterial electronics for bio-embodied intelligence.

METHODS

Fabrication of multiple 3D FMs

A general process of BμSL was used for the preparation and formation of multiple 3D FMs, as shown in [Figures S1](#), [S7](#), and [S8](#). However, for the 3D hydrogel, aerogel, and liquid metal, the surface of W had to undergo a pre-treatment. In addition, during material removal, a high-pressure atmosphere

of linear hydrocarbons was selected, and it was used for W removal at constant temperature ([Note S2](#)). The pre-process of BμSL comprised three steps. Firstly, PMs were fully coated by the liquid wax in a vacuum environment to discharge air bubbles when the wax was heated to 60°C. Then, the hollow W was cleaned via electrowetting with a polar solvent for 20 s and dried. After injecting FMs into the cavity of W, unless otherwise specified, the default W removal consisted of drying the 3D FM at 75°C for 12 h.

To print the soluble PM, we utilized a high-resolution (bottom-top printing, up to 10 μm) projection micro-stereolithography tech (PμSL) based on the customized vat 3DP system (Nano Arch P140, BMF Material Technology). Each designed computer-aided design (CAD) model was sliced layer by layer with a suitable thickness, ensuring that the explosion parameters could be precisely adjusted as shown in [Figures S2C–S2F](#). The printing platform always remained horizontal, and the liquid resin was updated in real time when the platform was raised or lowered. Within the first 10 layers of projection, UV-light energy should be adjusted by the exposed area and substrate adhesion, and this ensures that the firm attachment of the cured part to the platform is not stuck. After continuous 3DP, PMs were post-processed to ensure good accuracy for aimed structural resolution.

Electrowetting and injection in ultra-hydrophobicity microchannels

An external electric field can affect the inner energy (ΔF_a) fluctuation of the droplet, which is calculated by subtracting the surface energy (F_s) from the electrostatic free energy (F_e), upon contact with the inner wall of W (expressed in [Note S3](#)). The variation in the shape of a droplet under an electric field is caused by changes to ΔF_a , whose oscillatory vectors maintain the same phase as the electric field. Droplets in microtubes can passively undergo electric field manipulation and achieve complete wetting and flushing of the micropores in the interior. Furthermore, when PM reaches an aspect ratio of 20, the composited mold should be immersed in the solution and repeatedly scour the hollowed W through the mechanical pump to achieve a complete removal. The analytical model of the continuous injection is expressed by the normal hydraulic model ([Note S4](#)). The filling volume (Q) in the channel with radius r can be expressed as

$$Q = \int_V \frac{\pi \rho r^4}{8\mu^3 v} \left(\Delta P - \frac{\pi r^2}{G(t) \sin \alpha + F_{in}} \right) dV,$$

where G(t) is the liquid effective gravity, α is the inclination angle of the channel, ρ is the solution density, and μ and ν are the dynamic and kinematic viscosity, respectively. We focused on ideal circular micropipes, where Q(t) increases while the rate ∂Q(t) decreases over time. The length of the flow path decreases with time, causing a gradual decrease in velocity (u). Therefore, the greater the ΔP, the higher the Q and the shorter time it takes to reach saturation. In experiments, we used a cured silicone rubber seal and immobilized the W thoroughly. The mold was securely fixed within a filtration pipette, and the parameters were meticulously adjusted to ensure filling and demolding.

Programmed FMP_x design

The electric displacement (D_n) along the principal strain direction is derived from the volume integration within the principal stress space of the unit cell. We developed the theoretical dielectric model for the relationship between the piezoelectric charge constant matrix, d_{nk} , and D_n . We demonstrate that due to the presence of the angle α , structures with different orientations and size parameters give rise to tunable voltage results (Note S5). The output voltage of the U_{3n} devices can be determined from the piezoelectric voltage constant g_{3n} (with the local value, g_{nk}) of the composites and the strain ϵ_{nk} of the design units as follows:

$$U_{3n} = \int_{V_i} g_{nk} \epsilon_{nk} E_p dV_i.$$

Special considerations should be made such that, under high pressure, the response of FMs after reaching their deformation limit is proportional to their mass, like FMP₁, while under low pressure, the response is proportional to the volume integral of ϵ_{nk} in the global system.

Characterization

FM samples were imaged via SEM (SU8010, Hitachi) at an accelerating voltage of 8–20 kV. The constituent elements on FM surfaces were analyzed by energy-dispersive X-ray spectroscopy (EDS), which was performed with an applied voltage of 10–20 kV. The applied voltage was selected to ensure the greatest accuracy when quantifying the nanocomposite elements (Figure S1). To prove the complete removal of residual PMs, we used Cu ions grafted onto acid groups as the probes in resin, which showed no adhesion to the interior of W in the energy dispersive spectrum (EDS) switched to the mapping mode. Boron nitride (BN) was dispersed in deionized (DI) water, and the uniform dispersion was taken from the supernatant after centrifugal treatment at 8,000 rpm, 30 min, which was characterized for transmission electron microscopy (TEM) by using a lift-out procedure in an SEM (S9500, Hitachi) within a high magnification (Figures 3C and S10). Lamellae of PVA/BNNS with a thickness of less than 100 nm were prepared for TEM and cross-section for characterization through the brittle break at an extremely low temperature while immersed in liquid nitrogen. TEM imaging was performed with a JEM-2800 (Jeol) transmission electron microscope with a 200 kV beam.

Measurement and performance testing

The upper and lower planes of the sample were artificially set as planes during molding to facilitate the transmission of the positive pressure in the compression test. The universal mechanical properties were performed and measured on a universal testing machine (INSTRON, MicroTester 5848). As a motion platform created to demonstrate the performance of FMP_x, BASS was performed for different grab and move actions by a small-size customized collaborative robotic arm (UR3e, Universal Robots USA). The packaging procedures for polarization are detailed in Note S5. The voltage for polarization was supplied by an amplifier/controller (TREK 610E H.V.) to ensure the electric poling process. The piezoelectric outputs were evaluated by an analyzed system consisting of an electromechanical vibrator,

function generator, and oscilloscope. A Tektronix DPO 3034 oscilloscope with a 100 MΩ probe was used to measure the open-circuit piezoelectric voltage.

RESOURCE AVAILABILITY

Lead contact

Further information and requests for resources should be directed to and will be fulfilled by the lead contact, Xiaoming Chen (xiaomingchen@xjtu.edu.cn).

Materials availability

Most components of the soluble resin materials were purchased from McLean Tech. and synthesized following the steps detailed in Note S1. Most constituent matrices for the 3D FMs were purchased from Aladdin Biochemical Tech. and used as received: PDMS, Texoflex polyurethane (TPU), epoxy resin, and polyamide curing agent 651. Gallinstan (Ga-In) consisted of a homogeneous mixture of 75.5 wt % Ga and 24.5 wt % In and was purchased from Sino Sentech Material Tech. Sodium hydroxide, dimethyl-silicone oil (isolated), and calcium chloride (CaCl₂) were supplied by Sigma-Aldrich and used as received.

Most of the nanomaterials used for 3D FMs were purchased from Nanjing XFNANO Materials Tech. and used as received: a multi-walled CNT with an average outer diameter of 20 nm, iron nanoparticles (average diameter of 500 nm), and BTO nanoparticles (average outer diameter of 5–10 μm). BN powders with an average size of 13 μm, as the precursor of the piezoelectric nano-partial BNNS, were purchased from Momentive (USA). Commercial PVDF powders with an average diameter of 1 μm were purchased from Piezotech Arkema Group (France). Rubber was synthesized using a tin-catalyzed silicone elastomer mold max NV14 (matrix) and 10T (curing agent) from Smooth-on (USA).

Data and code availability

Data availability statements and the 3DP model (Datas S1–S12) are presented in the main text or the [supplemental information](#) files. The database used and figures analyzed during the current study are available from the corresponding author upon reasonable request.

ACKNOWLEDGMENTS

The authors gratefully acknowledge support from the National Natural Science Foundation of China (NSFC) (nos. 52175544 and 52172098), the National Key R&D Program of Shaanxi Province (nos. 2022GXLYH-01-12, 2023-GHZD-11, and 2023QCY-LL-26), and the Featured Research Base Project of the Xi'an Science and Technology Bureau(grant no. 23TSPT0001). The authors thank the useful Instrument Analysis Center of Xi'an Jiaotong University (XJTU) for the SEM, EDS, and ferroelectric test work and Dr. Jiao Li for the crystallographic TEM characterization of BNNS. The authors also wish to acknowledge Prof. Weiqiang Zhang (Xidian University) for the universal microscale tensile test system. The authors would like to thank Prof. Anbang Sun (XJTU) for the high-power pulse power for polarization.

AUTHOR CONTRIBUTIONS

Xiaoming Chen directed and conceived this research; Chunjiang Wang and Xiaoming Chen cleared and set up the BμSL methodology; Chunjiang Wang, Q.S., M.L., and D.M. explored the soluble resin and high-performance flexible piezoelectric composites; J. Shi, X.L., and Xiaoliang Chen designed the metamaterial; H.T. and Chunhui Wang performed the theoretical model of electro-wetting and simulation in microfluids; Chunjiang Wang expressed the mechanical behavior and programmed the response of FMP_x; Y.L. and J. Shao discussed the visualization of the biometric e-skin; Chunjiang Wang wrote the paper; and Xiaoming Chen and J.Z. reviewed and supervised this research. All authors discussed and commented on the manuscript.

DECLARATION OF INTERESTS

The authors declare that they have no competing interests.

SUPPLEMENTAL INFORMATION

Supplemental information can be found online at <https://doi.org/10.1016/j.device.2024.100658>.

Received: August 29, 2024

Revised: November 28, 2024

Accepted: December 12, 2024

Published: January 9, 2025

REFERENCES

- Chortos, A., Liu, J., and Bao, Z. (2016). Pursuing prosthetic electronic skin. *Nat. Mater.* 15, 937–950. <https://doi.org/10.1038/nmat4671>.
- Chandrasekaran, S., Lin, D., Li, Y., and Worsley, M.A. (2023). Aerogels, additive manufacturing, and energy storage. *Joule* 7, 866–883. <https://doi.org/10.1016/j.joule.2023.03.021>.
- Roh, Y., Lee, S., Won, S.M., Hwang, S., Gong, D., Kim, C., Hong, I., Lim, D., Kim, H., Kim, M., et al. (2023). Crumple-recoverable electronics based on plastic to elastic deformation transitions. *Nat. Electron.* 7, 66–76. <https://doi.org/10.1038/s41928-023-01089-6>.
- Lu, M., Huang, C., Xu, Z., Yuan, Y., Wang, M., Xiao, M., Zhang, L., and Wan, P. (2023). A Skin-Bioinspired Urchin-Like Microstructure-Contained Photothermal-Therapy Flexible Electronics for Ultrasensitive Human-Interactive Sensing. *Adv. Funct. Mater.* 33, 2306591. <https://doi.org/10.1002/adfm.202306591>.
- Zhou, Q., Ji, B., Hu, F., Dai, Z., Ding, S., Yang, H., Zhong, J., Qiao, Y., Zhou, J., Luo, J., and Zhou, B. (2022). Magnetized Microcilia Array-Based Self-Powered Electronic Skin for Micro-Scaled 3D Morphology Recognition and High-capacity Communication. *Adv. Funct. Mater.* 32, 2208120. <https://doi.org/10.1002/adfm.202208120>.
- Wang, Y., Xu, C., Yu, X., Zhang, H., and Han, M. (2022). Multilayer flexible electronics: Manufacturing approaches and applications. *Mater. Today Phys.* 23, 100647. <https://doi.org/10.1016/j.mtphys.2022.100647>.
- Chen, J., Zhu, Y., Chang, X., Pan, D., Song, G., Guo, Z., and Naik, N. (2021). Recent Progress in Essential Functions of Soft Electronic Skin. *Adv. Funct. Mater.* 31, 2104686. <https://doi.org/10.1002/adfm.202104686>.
- Wang, Y., Liang, J., Yu, J., Shan, Y., Huang, X., Lin, W., Pan, Q., Zhang, T., Zhang, Z., Gao, Y., et al. (2024). Multiscale haptic interfaces for metaverse. *Device* 2, 100326. <https://doi.org/10.1016/j.device.2024.100326>.
- Jiang, S., Liu, X., Liu, J., Ye, D., Duan, Y., Li, K., Yin, Z., and Huang, Y. (2022). Flexible Metamaterial Electronics. *Adv. Mater.* 34, 2200070. <https://doi.org/10.1002/adma.202200070>.
- Dai, S., Dai, Y., Zhao, Z., Xia, F., Li, Y., Liu, Y., Cheng, P., Strzalka, J., Li, S., Li, N., et al. (2022). Intrinsically stretchable neuromorphic devices for on-body processing of health data with artificial intelligence. *Matter* 5, 3375–3390. <https://doi.org/10.1016/j.matt.2022.07.016>.
- Lee, J., Lim, D.D., Park, J., Lee, J., Noh, D., Gu, G.X., and Choi, W. (2023). Multifunctionality of Additively Manufactured Kelvin Foam for Electromagnetic Wave Absorption and Load Bearing. *Small* 19, 2305005. <https://doi.org/10.1002/smll.202305005>.
- Lee, J., Han, H., Noh, D., Lee, J., Lim, D.D., Park, J., Gu, G.X., and Choi, W. (2024). Multiscale Porous Architecture Consisting of Graphene Aerogels and Metastructures Enabling Robust Thermal and Mechanical Functionalities of Phase Change Materials. *Adv. Funct. Mater.* 34, 2405625. <https://doi.org/10.1002/adfm.202405625>.
- Sinha, P., and Mukhopadhyay, T. (2023). Programmable multi-physical mechanics of mechanical metamaterials. *Mater. Sci. Eng. R* 155, 100745. <https://doi.org/10.1016/j.mser.2023.100745>.
- Malek, C.K., and Saile, V. (2004). Applications of LIGA technology to precision manufacturing of high-aspect-ratio micro-components and -systems: a review. *Microelectronics. J.* 35, 131–143. <https://doi.org/10.1016/j.mejo.2003.10.003>.
- Yan, Y., Liu, X., Yan, J., Guan, C., and Wang, J. (2021). Electrospun Nanofibers for New Generation Flexible Energy Storage. *Energy. Environ. Mater.* 4, 502–521. <https://doi.org/10.1002/eem2.12146>.
- Rogers, J.A. (2010). Electronics: A diverse printed future. *Nature* 468, 177–178. <https://doi.org/10.1038/468177a>.
- Liu, D., Wan, J., Pang, G., and Tang, Z. (2019). Hollow Metal–Organic-Framework Micro/Nanostructures and their Derivatives: Emerging Multi-functional Materials. *Adv. Mater.* 31, 1803291. <https://doi.org/10.1002/adma.201803291>.
- Zheng, X., Lee, H., Weisgraber, T.H., Shusteff, M., DeOtto, J., Duoss, E.B., Kuntz, J.D., Biener, M.M., Ge, Q., Jackson, J.A., et al. (2014). Ultralight, ultrastiff mechanical metamaterials. *Science* 344, 1373–1377. <https://doi.org/10.1126/science.1252291>.
- Hu, Y., Guo, Z., Ragonese, A., Zhu, T., Khuje, S., Li, C., Grossman, J.C., Zhou, C., Nouh, M., and Ren, S. (2020). A 3D-printed molecular ferroelectric metamaterial. *Proc. Natl. Acad. Sci. USA* 117, 27204–27210. <https://doi.org/10.1073/pnas.2013934117>.
- Ren, J., Zhang, Y., Zhao, D., Chen, Y., Guan, S., Liu, Y., Liu, L., Peng, S., Kong, F., Poplawsky, J.D., et al. (2022). Strong yet ductile nanolamellar high-entropy alloys by additive manufacturing. *Nature* 608, 62–68. <https://doi.org/10.1038/s41586-022-04914-8>.
- Zhang, Q., Zhang, F., Xu, X., Zhou, C., and Lin, D. (2018). Three-Dimensional Printing Hollow Polymer Template-Mediated Graphene Lattices with Tailorable Architectures and Multifunctional Properties. *ACS Nano* 12, 1096–1106. <https://doi.org/10.1021/acsnano.7b06095>.
- Ye, J., Liu, L., Oakdale, J., Lefebvre, J., Bhowmick, S., Voisin, T., Roehling, J.D., Smith, W.L., Cerón, M.R., van Ham, J., et al. (2021). Ultra-low-density digitally architected carbon with a strutted tube-in-tube structure. *Nat. Mater.* 20, 1498–1505. <https://doi.org/10.1038/s41563-021-01125-w>.
- Ligon, S.C., Liska, R., Stampfl, J., Gurr, M., and Mülhaupt, R. (2017). Polymers for 3D Printing and Customized Additive Manufacturing. *Chem. Rev.* 117, 10212–10290. <https://doi.org/10.1021/cacs.chemrev.7b00074>.
- Patel, D.K., Sakhai, A.H., Layani, M., Zhang, B., Ge, Q., and Magdassi, S. (2017). Highly Stretchable and UV Curable Elastomers for Digital Light Processing Based 3D Printing. *SP. Adv. Mater.* 29, 1606000. <https://doi.org/10.1002/adma.201606000>.
- Ho, D.H., Hong, P., Han, J.T., Kim, S.Y., Kwon, S.J., and Cho, J.H. (2020). 3D-Printed Sugar Scaffold for High-Precision and Highly Sensitive Active and Passive Wearable Sensors. *Adv. Sci. N. S.* 7, 1902521. <https://doi.org/10.1002/advs.201902521>.
- Davoodi, E., Montazerian, H., Haghniaz, R., Rashidi, A., Ahadian, S., Sheikhi, A., Chen, J., Khademhosseini, A., Milani, A.S., Hoofar, M., and Toyserkani, E. (2020). 3D-Printed Ultra-Robust Surface-Doped Porous Silicone Sensors for Wearable Biomonitoring. *ACS Nano* 14, 1520–1532. <https://doi.org/10.1021/acsnano.9b06283>.
- Kim, F., Yang, S.E., Ju, H., Choo, S., Lee, J., Kim, G., Jung, S.H., Kim, S., Cha, C., Kim, K.T., et al. (2021). Direct ink writing of three-dimensional thermoelectric microarchitectures. *Nat. Electron.* 4, 579–587. <https://doi.org/10.1038/s41928-021-00622-9>.
- Liska, R., Schwager, F., Maier, C., Cano-Vives, R., and Stampfl, J. (2005). Water-soluble photopolymers for rapid prototyping of cellular materials. *J. Appl. Polym. Sci.* 97, 2286–2298. <https://doi.org/10.1002/app.22025>.
- Peng, S., Wang, Z., Lin, J., Miao, J., Zheng, L., Yang, Z., Weng, Z., and Wu, L. (2020). Tailored and Highly Stretchable Sensor Prepared by Crosslinking an Enhanced 3D Printed UV-Curable Sacrificial Mold. *Adv. Funct. Mater.* 31, 2008729. <https://doi.org/10.1002/adfm.202008729>.
- Xue, J., Gao, L., Hu, X., Cao, K., Zhou, W., Wang, W., and Lu, Y. (2019). Stereolithographic 3D Printing-Based Hierarchically Cellular Lattices for High-Performance Quasi-Solid Supercapacitor. *Nano-Micro Lett.* 11, 46. <https://doi.org/10.1007/s40820-019-0280-2>.
- Wilts, E.M., Pekkanen, A.M., White, B.T., Meenakshisundaram, V., Aduba, D.C., Williams, C.B., and Long, T.E. (2019). Vat photopolymerization of

- charged monomers: 3D printing with supramolecular interactions. *Polym. Chem.* 10, 1442–1451. <https://doi.org/10.1039/C8PY01792A>.
32. Schuster, M., Inführ, R., Turecek, C., Stampfl, J., Varga, F., and Liska, R. (2006). Photopolymers for rapid prototyping of soluble mold materials and molding of cellular biomaterials. *Monatshefte. fur. Chemie* 137, 843–853. <https://doi.org/10.1007/s00706-006-0484-2>.
33. Johansson, R.S., and Vallbo, A.B. (1979). Tactile sensibility in the human hand: relative and absolute densities of four types of mechanoreceptive units in glabrous skin. *J. Physiol.* 286, 283–300. <https://doi.org/10.1113/jphysiol.1979.sp012619>.
34. Sun, C., Li, D., Liu, T., An, Q., Zhang, C., Li, Y., and Liao, W. (2024). Design of functionally gradient metastructure with ultra-broadband and strong absorption. *Compos. Part B. Eng.* 280, 111484. <https://doi.org/10.1016/j.compositesb.2024.111484>.
35. Wang, Y., Wu, H., Li, T., Wang, J., Wei, Z., and Wang, H. (2024). Toward human-like touch sense via a bioinspired soft finger with self-decoupled bending and force sensing. *Cell Rep. Phys. Sci.* 5, 102225. <https://doi.org/10.1016/j.xcrp.2024.102225>.
36. Lim, D.D., Park, J., Lee, J., Noh, D., Lee, J., Choi, J., and Choi, W. (2022). Broadband mechanical metamaterial absorber enabled by fused filament fabrication 3D printing. *Addit. Manuf.* 55, 102856. <https://doi.org/10.1016/j.addma.2022.102856>.
37. Wang, W., Jiang, Y., Zhong, D., Zhang, Z., Choudhury, S., Lai, J.-C., Gong, H., Niu, S., Yan, X., Zheng, Y., et al. (2023). Neuromorphic sensorimotor loop embodied by monolithically integrated, low-voltage, soft e-skin. *Science* 380, 735–742. <https://doi.org/10.1126/science.adc0086>.

Supplemental information

**Investment micro-casting 3D-printed
multi-metamaterial for programmable
multimodal biomimetic electronics**

Chunjiang Wang, Xiaoming Chen, Qihang Song, Jianxu Shi, Mengyong Lei, Duo Ma, Xiangming Li, Xiaoliang Chen, Hongmiao Tian, Chunhui Wang, Jie Zhang, Yang Lu, and Jinyou Shao

TABLE OF CONTENTS.

Supplemental Notes S1–S6.

- Note S1 Micro–stereolithography projection of soluble resin.
- Note S2 Process of multiple 3D metamaterials via B μ SL.
- Note S3 Analytical model of electronic–wetting assisted dissolution.
- Note S4 Derivation of flow model in an ideal microtube.
- Note S5 Design, fabrication, and responses of FMP.
- Note S6 Response and reinforcement learning of BASS.

Supplemental Figures S1–S16.

- Figure S1. Characteristics of multiple 3D FMs.
- Figure S2. Principle of 3DP soluble resin.
- Figure S3. Cross–scaled forming capability of PM.
- Figure S4. Three printing samples to achieve extreme features.
- Figure S5. Simulation and experiments of PM dissolution.
- Figure S6. Processes and results of continuous filling.
- Figure S7. Multi-material deposition 3D FM.
- Figure S8. Comparison diagram of micro–3D forming methods.
- Figure S9. Design models and FEA of 3D FMP_x.
- Figure S10. Fabrication and compression texturing of 3D FMP.
- Figure S11. Polarization and dielectric measurement of 3D FMP.
- Figure S12. Piezoelectrical responses and stability of FMG–T/J.
- Figure S13. Output features in stiffness, friction, and loading of FMG–T/J.
- Figure S14. Signal acquisition and training logic of BASS.
- Figure S15. Grabbing different rigidity fruits via BASS.
- Figure S16. Comprehensive performance comparison of the typical soft fingers reported in the literature.

Supplemental Tables S1–S4.

- Table S1. Forming capabilities of the other removable materials compared in Figure 2H.
- Table S2. Other 3DP methods for multiple 3D metamaterials.
- Table S3. Compared features to this approach, B μ SL.
- Table S4. Performance comparison of bioinspired soft fingers reported in the literature

SUPPLEMENTAL NOTES

Note S1 Micro-stereolithography projection of soluble resin.

Resin materials.

The following reagents were employed for the synthesis of soluble resin compounds and intermediate resin compounds in B_μSL, which were used as received: N,N-dimethylacrylamide (DMA) stabilized with MEHQ, methacrylic acid (MA), methacrylic anhydride (MAA), Sudan(I), polyvinylpyrrolidone (PVP, Mn~10000), 1-(4-methoxyphenyl)-3-(4-tert-butylphenyl)-1,3-propane Dione (Avobenzone), 1-hydroxy cyclohexyl phenyl ketone (Irg184), phenylbis (2,4,6-trimethyl benzoyl) phosphine oxide (Irg819), and poly(vinyl alcohol) (PVA, alcoholysis degree 98.0–99.0 mol%).

Resin formulations.

Curing monomers were composed of 175 g DMA with MEHQ, 175 g MA and 75 g MAA. Filling agents were a mixture of PVA and PVP with a ratio of 1:1 for crosslinking mechanical reinforcement. Light indicator agent is I819/I184 blend (1:1).

Resin preparation.

Several kinds of reaction monomers were stirred at room temperature for half an hour at the speed of 1000 rpm. Other powdered fillers were slowly added to the resin in a 45 °C water bath and stirred at 750 rpm until the liquid was clear and transparent. The soluble resin was stored and used in an anaerobic atmosphere and dark room.

Soluble resin μ-3DP.

The synthesized soluble photosensitive resin was introduced into a liquid tank and evenly covered on a horizontal membrane frame. Transparent Teflon membrane was positioned horizontally at a predetermined distance beneath the film, to make an anaerobic zone below the resin for continual separation with next layer. Upon descending the specified distance, the layered resin was exposed to digital 2D light pattern, enabling the completion of the multi-step curing process. Cured pre-molds (PMs) should not be immersed in liquid for at least 5 minutes to prevent formation of semi-crosslinking on surfaces because of similar compatibility. The process was repeated and finally, the layered cured resin was incorporated into the pre-designed PMs.

Sample post treatment.

Once the PM was successfully solidified, it was removed from build substrate, cleaned in absolute alcohol, dried under flowing air and secondary cured in UV lamp oven at 75°C for 20 min. Finally, samples were placed into vacuum drying storage dishes for coating wax.

Note S2 Process of multiple 3D metamaterials via B_μSL.

Material preparation for 3D nanocomposite composed FMs.

The dispersion uniformity of the composite 3D FMs was characterized using SEM. Results were obtained for microstructure dispersion, size changes, and EDS elemental distribution (low-resolution

scanning in Figure S1A). It was found that four typical composites maintained FMs uniformity before and after B μ SL, with no apparent agglomeration or layering phenomena. This result indicates that the resolution error of the 3D structure could be regulated within a reasonable range.

In B μ SL, the demolding and injection method is very suitable for molding composite materials with thermosetting substrates, for example: PDMS, PU, SE, and epoxy, which were achieved in Figure S1. It is also the main reason why the component selected as BNNS/SE in the demo of this article. Thermoplastic materials (like PI, plastic powder) can also be molded via B μ SL within a reasonable melting temperature. As a stricter prerequisite, the removal processes among FM and templates were inevitably challenged; for instance, organic immersion and acid etching should be isolated to avoid reaction with FM for phase separation.

Moreover, the processes limitation involves adjustment of the temperature difference during the twice Boolean-inversion operations. The prerequisite that can be determined is that the phase change temperature of the paraffin mold (W) needs to add nanofillers or change the paraffin polymer to withstand the injection molding of thermoplastic materials. For the removal of this type of paraffin, it is demanded to apply the polar organic solvent (like petroleum, alkanes and so on) to dissolve it instead of simply heating it.

2.5D PDMS FM. PDMS monomer and curing agent were mixed in a ratio of 10:1 and used within 30 min after preparation (Figure 2B).

3D PDMS–Fe FM. The composites consisted of 8.6 g Fe nanoparticles in 1.4 g PDMS–curing matrix, which were mixed and used within 1 min after preparation. The same methods for preparing this kind of material are listed in Figure 1C focused on solid content^{1–4}.

3D Epoxy–BTO FM. Epoxy composites, consisting of 9.2 g BTO nanoparticles in 0.8 g epoxy and 0.1 g curing agents, were fully mixed and used with 15 min after preparation. For comparison, the same methods are listed in Figure 1C focused on solid content^{5–7}.

3D PDMS–BTO FM. The composites consisted of 9.2 g BTO nanoparticles in 0.8 g epoxy matrix and 1 g curing agent, which were well mixed by stirring rod at 500 rpm, and used within 1 min after preparation, as shown in Figure 1D.

3D elastomer–CNT FM. Firstly, 2 g MWCNTs were dispersed into 500 mL aqueous solution to obtain the 400 mg/mL concentration. Then, 0.25 g MWCNTs and 20 g elastomer were compounded according to the ratio of 15% CNT by stirring in water bath at 75°C and evaporating with magneton side. The mixtures and curing agents were mixed in a ratio of 10:1 after preparation (Figure 1C).

Material preparation for hydrogel, aerogel, and liquid metal composed of FMs.

3D Ga–In FM. Ga–In alloy was heated and used for filling. FM should be stored below 25°C and was used as received; its paraffin content was removed by polar organic solvents, such as petroleum, xylene, etc. For molding various liquid metals with various melting points, the content of paraffin, whose melting point is higher than that of the metal, should be adjusted (low-resolution scanning in SEM was shown in Figure S1B). As comparison, the other methods^{7–10} focused on forming accuracy are listed below

Figure 1C.

3D hydrogel FM. Herein, 12 g anhydrous calcium chloride powder was dissolved in 100 g of deionized water. Then, alginate powder (used as received) with overall content of 1.5%, 5% and 10% was added to deionized water under magnetic stirring at 45°C, and then cooled to room temperature. Sodium alginate solution was poured into the hollowed wax template (W) without any bubbles at 15°C. The transparent FW was completely infiltrated in calcium oxide solution at 4°C for 12 h to allow the gelation of calcium alginate (low-resolution scanning in SEM was shown in Figure S1B). The other methods^{11–14} to form the 3D hydrogel focused on forming accuracy are shown in Figure 1C.

3D TPU/BNNS aerogel FM. Commercial BN micro-powder was dispersed into a mixed solvent of isopropanol and DI with the mass ratio of 1:1. The resulting dispersion was centrifuged successively at 2500 rpm for 5 min and 9500 rpm for 20 min, followed by freeze-drying to obtain exfoliated BNNSs. The TPU precursor was prepared by uniformly mixing 6 g TPU pellets and 100 mL DMF-based BNNSs solvent with rapid stirring at 60°C. The mixture was added into W and placed in a –25°C freezer for 24 h. The FW was then transferred to a freeze-drying vessel at –80°C for 72 h below 4 Pa. After that, the hollowed 3D aerogel FM was formed under hot air flow at 70°C for 2 h (Figure 1C).

3D PVA/BNNS aerogel FM. First, 2 g BNNSs and 1 g PVA powder were mixed in 30 g DI and sonicated at 200 W for 30 min. The composite was filled in the hollowed W and placed in a –25°C freezer for 24 h (Figure 3C).

Principle of the 3DP for soluble resin.

The main constituents of the soluble photosensitive resin were N,N-dimethylacrylamide (DMA) and methacrylic acid (MAA), as the primary monomers for curing crosslinked network referred by the previous work¹⁵ (Figure 2A). Upon photon excitement, only a minor portion of the double bonds in these two monomers underwent opening, resulting in a diminished formation of crosslinked long polymer chains (Figure S2A). Consequently, there were not enough embedded positions between adjacent curing chains to establish an interconnected network.

The photosensitive peak positions within the range of 330–350 nm was controlled using a visible–UV spectrometer (UV–3600, Shimadzu Corporation) when manipulating the substrate compositions. Related sensitive peaks of the four monomers and their combinations were observed in the visible–UV spectrometer instrument. To adapt the resin to the working range of the printer, fillers such as I819, I184, and a light-blocking agent were added to facilitate UV reaction at wavelength of 405 nm. A localized peak at 401 nm was regulated, as shown in Figure S2B.

Photocuring properties of the soluble resin.

The influence of light intensity and exposure time on the curing thickness was assessed by quantitatively controlling these parameters during the photopolymerization on a logarithmic coordinate system (Figure S2C). As the light intensity increased, the exposure time was lengthened, and the curing depth of the resin was deepened. The photosensitive characteristics of the resin were found to adhere to the Beer–Lambert absorption law¹⁶, as expressed in equation 1:

$$C_d = D_d \ln\left(\frac{E_m}{E_c}\right) \quad (\text{Equation 1})$$

In the above formula, D_d represents the depth of curing, E_m is the energy absorbed during UV irradiation, and E_c is the critical threshold energy of resin defined by absorption, diffusion, and other intrinsic coefficients. The curing light depth was controlled by the incorporation of a photo-inhibitor to completely impede the diffusion of photopolymerization radicals (Figure S2C). It led to a significant reduction of thickness to 1/20 of the value observed without the presence of photo-inhibitor. During continuous printing, the thickness of the cured layers remained consistent, as demonstrated in Video S2. Each adjacent layer can be bonded together through overlapping regions, facilitating the accumulation of subsequent layers and the formation of the desired 3D FMs.

Capability of soluble PM for cross-scale BμSL process.

BμSL was employed to indirectly form pyramid-shaped protrusion templates on a low-dimensional thick and flexible film, with feature dimensions of 20 μm. The heights of these micro-features were scanned using laser confocal microscopy, which revealed that the deviations of the 2.5D micro-protrusion from the design dimensions were less than 2% in both the horizontal and depth directions (Figure S3A). Distinctive concave pit structures were formed on the PDMS film mold and set on the surface of the silicon wafer (as characterized by SEM images in Figure 2C). These results indicate that the inherent stretchability of this resin has good potential for further applications, such as low-dimensional template-indicated imprinting and creation of highly flexible electronic skins (Figure S3B).

For the fabrication of cross-scaled 3D micro-molds, superlattice structures were designed with minimum dimensions of 20 μm and maximum dimensions of 4 cm. Under SEM observation, the dimensional error of the 3D PM was found to be less than 3%, exhibiting smooth surfaces and complete structural integrity (Figure S3C). To address variations in exposure field, the printing parameters were adjusted, enabling the manufacturing of diamond superlattices with a precision of 100 μm at the macroscopic scales of 1 cm and 10 cm (Figures S3D–S3E). The main difference in the photopolymerization for various sizes and shapes of PMs lies in the residence time of PM in the resin vat. It is crucial for BμSL to applied for an acoustic 3D FM (Figure S3F), which has a larger macro size and smaller micro features, given its ability to be quickly printed without obviously detects. The typical dimension of the device which was suitable for printing reached 25 cm and the minimum resolution reached 125 μm.

Note S3 Analytical model of electronic-wetting assisted dissolution.

Analytical physical model of electrowetting in micro-channel.

In the initial state, the water droplet theoretical model shows a linear relationship between the contact angle (CA), θ , and the surface tension γ_{ij} as follows equation (2) by Young's equation:

$$\gamma_{sa} = \gamma_{sl} - \gamma_{la} \cos \theta \quad (\text{Equation 2})$$

where γ_{sa} is the surface energy between the wax and air, γ_{sl} is the surface energy between the wax and liquid, γ_{la} is the surface energy between the liquid and air. Applying a spatial electric field (E_a) both side of the mold, the triple-phase CA of the droplet should be expressed via Young–Lippmann equation as follows:

$$\cos \theta_v = \cos \theta_0 + \frac{E_a^2}{2c} \epsilon_0 \epsilon_r \gamma_{la} \quad (\text{Equation 3})$$

where γ_{la} refers the surface energy between the liquid and air; ϵ_0 refers to the permittivity in vacuum; ϵ_r refers to the permittivity in the droplet; c means the effective thickness of dielectric solid. Through applying the electric field, the surface tension of droplet between the hydrophobic wax and solution becomes much smaller, expressed by Lippmann equation as follows (4):

$$\gamma_{sl-E} = \gamma_{sl} - \frac{1}{2c} \epsilon_0 \epsilon_r^s E_a^2 \quad (\text{Equation 4})$$

The correlation between the change in voltage E_a and the CA, θ , following the combined formulation of equations (2) and (3) to unite the applied potential, is further described as an exact solution considering the law of conservation of energy. The decrease in liquid surface energy also indicates a decrease in the overall droplet energy, which can inevitably lead to changes in the droplet shape with voltage fluctuations. SEM images of resin obstruction within the micro–pores after dissolution are shown in Figures S5A–S5B, which gave rise to the crystallization of acrylic acid moieties due to incomplete dissolution. This phenomenon is mainly due to the uneven distribution of energy in photocuring region, resulting in variations in the polymerization density of the PM molecular chains. The surface energy F_s which is defined by equation (5):

$$F_s = (\gamma_{sl} - \gamma_{sa}) S_{ls} + \gamma_{la} S_{la} \quad (\text{Equation 5})$$

The change of free energy of droplet $\Delta F_a = F_s + F_e$ can affect the shape of droplet, and it also represents the total free energy of electrical, chemical, and surfaces in the liquid droplet. The electrostatic energy F_e is defined by equation (6):

$$F_e = \frac{1}{2} \int_{\text{droplet}} E_0 E_a (\epsilon_0 \epsilon_r^d - \epsilon_0 \epsilon_r^a) dV \quad (\text{Equation 6})$$

where ϵ_r^d and ϵ_r^a are the relative permittivity inner and outer of the droplet respectively; S_{la} and S_{ls} are the effective surfaces of the droplet in contact with air and wax respectively. Herein, the analytical solution was obtained in the case of $\theta = 90^\circ$ for a qualitative understanding of the physics behind the observed experimental phenomena, without considering numerical solutions in general.

The actual electrowetting effect inside was simulated using COMSOL Multiphysics (COMSOL Inc., Stockholm, Sweden). As illustrated in Figure S5C, The shape of droplet in the wax channel also was approximated as an ellipsoid with a long axis of H , a short axis of R , the eccentricity of e_r and geometrical factor n for the definite integral. Each droplet was unable to infiltrate the micro–channels, exhibiting a contact angle of 102.6° via experimental testing. When a constant spatial electric field of 20 kV/cm was

set, the wetting of droplets was restricted, resulting in a modified contact angle of 81.7°.

Divided by the central axis of the porous channel, the liquid on both sides exhibited a greater propensity for wetting, which was attributed to the fact that droplets located farther away from the central axis and required a larger volume to fill the channel. Closer regions to the axis experienced a dispersion of effective volume towards both sides, resulting in a parabolic-like trajectory connecting the filling endpoints.

Parameterized controlled electrowetting assisted process.

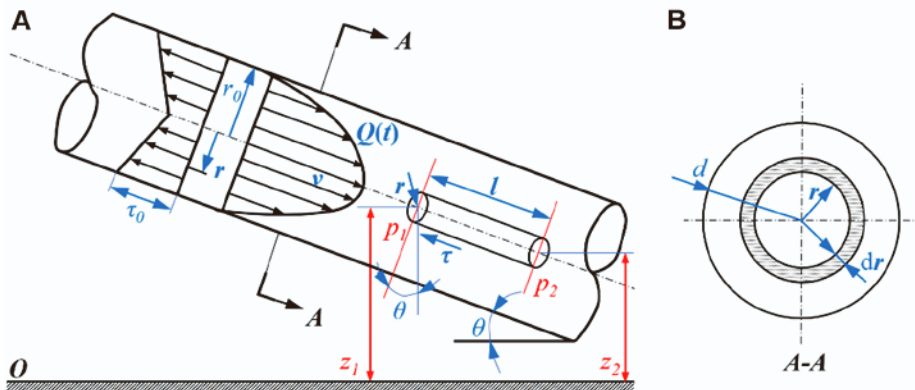
During the electrowetting experiment, the variations of CA between droplets and wax–wall can be observed using a contact angle measurement instrument (Video S3). The electric field magnitude and direction were regulated to achieve a repeated change in wetting. CA exhibited a linear variation and followed an opposite trend to the applied voltage, ranging from 91 to 97°.

Additionally, the dissolution solution was refreshed after carrying away the residual resin, as depicted in Figure S5D. Voltage fluctuations were implemented for over 2 hours at room temperature. Diamond structured 3D PM was employed as the vanished template, leading to the complete removal of PM in this case (Figure S5E). The hollow wax exhibited a smooth inner surface and a well-preserved architecture with an average groove width of 102.6 μm .

Note S4 Derivation of flow model in an ideal microtube.

Theoretical model of the liquid flow in microtube.

Force analysis was performed on the droplets within the microchannels. The motion of droplets is primarily driven by the differential pressure. The factors playing significant roles include pressure, viscous force (λ , dynamic viscosity of liquid, equal to $64/\text{Re}$ where Re is the Reynolds number), cohesion F_{in} by surface tension, and gravity G (Note Figure S1).



Note Figure S1. Diagram of theoretical model of FM filling in micro-tube. (A) Schematic diagram of the force distribution and moving status of the droplet in the ideal microfluidic channel. (B) Mathematic diagram of flow calculation for the droplet laminar flow in micro-hole from a cross-sectional perspective.

First, the method of infinitesimal elements was used for multitype force–balance analysis. The

existence of a laminar micro-cylinder was assumed with a length of dl inside the micro-channel. The pressure difference ΔP acting at the two ends of the ideal cylinder is directed towards the inner surface of the cylinder, and the pressures at the two ends are denoted as F_1 and F_2 , respectively. The direction of dr is the normal direction from the axis to the pipe wall, so it can be inferred that $dn=-dr$. Therefore, the tangential force T on the cylinder surface can be expressed as:

$$T = St = 2\pi lr \left(-\frac{\mu du}{dr} \right) = -2\pi\mu lr \frac{du}{dr} \quad (\text{Equation 7})$$

It may be inferred when the ideal liquid column was under pressure, the droplet in the center of ring was flown forward preferentially. By examining the force on dl , under the condition of steady laminar flow, the fluid segment with uniform motion has no axial force, obtained by formula (8).

$$\pi r^2 \Delta P + 2\pi rl\mu \frac{du}{dr} + G \sin \alpha = 0 \quad (\text{Equation 8})$$

Then adjusting the differential term, formula (8) can be written as:

$$u = \int_r^{r_0} -\frac{\rho gh_l}{2\mu l} r dr = -\frac{\rho gh_l}{4\mu l} r^2 + C \quad (\text{Equation 9})$$

By using the boundary conditions, the integral constant C can be determined. When $r=r_0$, the velocity u values to 0, so the radial velocity index in the laminar flow of the ideal pipe is expressed:

$$u = \frac{\rho gh_l}{4\mu l} (r_0^2 - r^2) \quad (\text{Equation 10})$$

here r_0 is the aperture of mold, r is the specific position radius at the flow rate. Radially, the velocity decreases following a parabolic function, with the maximum velocity $u = \rho gh_l / 4\mu l$ at the center position. This confirms that as the aperture of the micro-hole decreases, velocity u becomes slower. While the solution in the center of the ring flows backward due to the existence of viscous force h_l and cohesion F_{in} . The balance equation for the droplet can be given in formula (11).

$$\sum F = (\Delta P - h_l) S - G \sin \alpha - F_{in} = 0 \quad (\text{Equation 11})$$

When ΔP increases, the liquid will flow in the microchannel. In the analysis of Newtonian mechanics, upon traversing for a certain distance l , the droplet is wet the previously dry interior walls. It induces a pressure loss in traveled path as h_l , equaled to $\lambda l u^2 / 2gd$. There exists a critical pressure value ΔP_0 , and the filling rate can reach to 100% when the actual pressure exceeds it. The ideal analytical expression of ΔP_0 is followed in formula (12):

$$\Delta P_0 = \frac{G \sin \theta + F_{in}}{\pi r^2} + \frac{32\mu^3 l}{\rho d^2 u} \quad (\text{Equation 12})$$

Then, the flow volume can be expressed:

$$Q = \int_V \frac{\pi \rho r^4}{8\mu^3 u} \left(\Delta P - \frac{\pi r^2}{G(t) \sin \alpha + F_{in}} \right) dV \quad (\text{Equation 13})$$

Theoretical derivation of the filling rate in micro-channels.

On the other aspects, to determine the flow rate of laminar motion in a circular pipe in fluid mechanics, a liquid flow model is integrated at the cross-section of the microchannel. For any small circular ring with radius r and width dr on the original cross-section, the velocity at any point is u . The flow rate dq through the small area could be given by equation (14).

$$dq = 2\pi r u dr = \frac{\rho g h_l}{2\mu l} (r_0^2 - r^2) r dr \quad (\text{Equation 14})$$

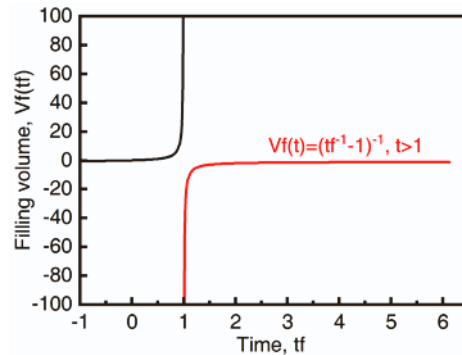
When the microchannel was set as horizontal, or the height difference ($z_1 - z_2$) at two ideal cross-sections was smaller than the pressure difference ($\Delta P/\rho g$) across the two cross-sections (which was often negligible in hydraulic pipelines). q could be written in standard fluid-kinetics notation (Hagen-Poiseuille equation), expressed in equation (15).

$$q = \frac{(p_1 - p_2)\pi d^4}{128\mu l} = \frac{\Delta P \pi d^4}{128\mu l}, \text{ and } q = \frac{\pi r^2 l}{t} \quad (\text{Equation 15})$$

In an ideal microchannel, the flow discharge and time of the ideal unit microcolumn obeyed the following impact correlation (equation 16). The ternary linear equation can be simplified as the equation (20) for the filling volume $V(t)$ without other variables besides t . $V(t)$ were set to be denoted as A , B , and C , respectively:

$$A = \frac{G \sin \theta + F_{in}}{\pi r^2}, \quad B = \frac{32\mu^3}{\rho d^2 u}, \quad C = \frac{128\mu l}{\pi d^4} \quad (\text{Equation 16})$$

$$V(t) = qt = \frac{C\pi r^2 At}{C\pi r^2 B t} = \frac{1}{\frac{1}{At} - \frac{B}{C\pi r^2 A}} \quad (\text{Equation 17})$$



Note Figure S2. Normalized curve. Normalized function curve after simplifying physical equation (16) of the filling volume $V_f(t_f)$ and time, t_f (no effective value in 1 s because of the existence of differences zero points under different parameters).

The above equation can be simplified as a function $f(x) = (t^1 - 1)^{-1}$, and the curve change trend in the first quadrant increases monotonically (Note Figure S2). Since the gravity of liquid in the microchannel also increases with the application, it is impossible to accurately measure the real-time gravity changes

in the ideal channel. At the same time, the volume value V in the overall filling needs to be integrated along the volume integral formula for the flow microtube of different spatial wax shapes. Due to the change for increasing $Gf(t)$ by t_f , the composite functions derived by an infinitesimal method can be approximated after integration in modifying model. In the filling experiment, the variation curve shown in Figure 3B is positively correlated with this theoretical model, which verifies the validity of the micropore infusion model.

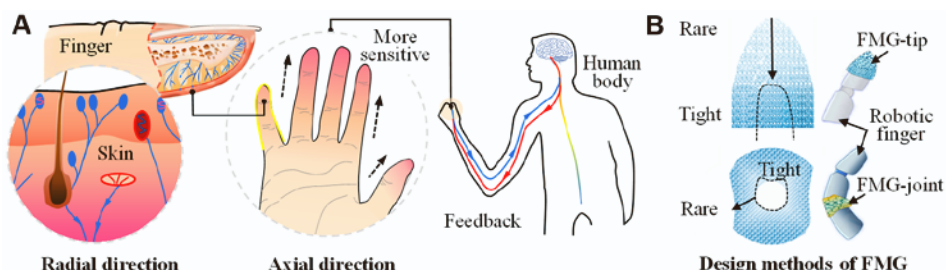
Filling process and experimental parameters.

By comparing the two schematic diagrams of the filling models in Figure S6A, the utilization of the top to bottom filling can ensure an alignment between the direction of air expulsion and composite material impregnation. Insufficient actual filling pressure may lead to incomplete removal of internal residual bubbles. As depicted in Figure S6B, a quantitative investigation was conducted on the relationship between the filling rate and the aspect ratio of spatial microtube. It was observed that a higher ΔP allowed for a wider range of fill width ratios (reaching up to 30). Similarly, when the porosity within the spatial microcavity mold reached 91%, complete filling can be achieved with a pressure differential of 30 kPa and a composite material viscosity of 500 cps (Figure S6C). A decrease in pressure led to a reduction in the effective filling volume within the same time frame.

The process of the silicon-based elastomer is illustrated in Figure S6D. PM with a design feature of 150 μm was fabricated, and its macroscopic dimensions were in the small size ($0.5 \times 0.5 \times 1 \text{ cm}$) and large size ($3 \times 3 \times 2 \text{ cm}$), respectively. After the resin dissolution, a hollow W was obtained with size of 142 μm . The surface was smooth without any burrs.

Note S5 Design, fabrication, and responses of FMP.

Principles of mechanical metamaterial inspired by finger nerves distribution.



Note Figure S3. Design strategy of biological FMP. (a) The distribution of the peripheral nerve along the axial and radial direction of fingers. (b) Design and layout of FMG-T/J.

The distribution of peripheral nerves on the human palm is depicted in Note Figure S3A. In terms of physiological structure, the peripheral nerves exhibit a gradient distribution from dense to sparse along the radial direction of the fingers, spanning from the superficial to the deep layers of the skin¹⁷. Similarly, in the vertical direction along the axis of the fingers, there is a predominance of nerve endings at the fingertips, while the posterior end primarily serves as a support area with fewer neurons dedicated to

force perception¹⁸.

As depicted in Note Figure S3B, the mechanical metamaterial FMP was arranged to enhance the performance of the robotic hand. Here, the tip one was positioned at fingertips (FMG-T), and the joint one was situated at the periphery (FMG-J).

Design and mechanical behavior of 3D FMP.

First, the basic lattice of piezoelectrical metamaterials was designed (Figure S9A). FMP was composed of optimized octagonal lattices defined with three parameter types. Its anti-carrying capacity was confirmed as the strongest among several patterns in the same volume (diamond, dot matrix, micro-column array, sphere, etc.). Three kinds of configuration were conceptualized with respective r values of 10, 8, and 6 (Figure S9B).

Composite process and characteristics of 3D FMP_x and FMG.

A solution containing 10% by mass of P(VDF-TrFE) and 10% of BNNS was dissolved in DMF. It was then treated in an ultrasonic bath at 50°C for 30 minutes at room temperature, followed by stirring in a water bath at 170°C until dried. Before curing, the mixture was degassed and spread evenly into a mold (thickness of 1 mm), yielding a uniform rubber-based P(VDF-TrFE)/BNNS composite material.

Furthermore, a complete FMG was fabricated via BuSL. These devices showcased a large size (5×5×2 cm), excellent flexibility, a smooth surface, and clear internal micro-features without obvious damage, as demonstrated in Video S4. Based on the EDS mappings and spectrums, the elements of FMG were found to be uniformly distributed in a random cross section, composed of C, O, B, and N. The surface displayed a consistent distribution without a clear deposition. Cross-sections of the FMG were taken and examined using an atomic force microscope in layer scanning mode (section e-1, e-2, and e-3). The height data indicated that the radial parameters of the rods under various design parameters were similar, which were uniformly dispersed on the surface.

Structural CAE analysis and typical mechanical response behavior.

The component of the effective piezoelectric charge constant d_{3n} in the principal stress direction of the 3D lattice is derived as follows:

$$d_{3n} = \frac{\overrightarrow{D}_n^{\text{eff}}}{\sigma_n^{\text{eff}}} = \frac{\sum_{i=1}^N \int_{V_i} d_{nk} \overrightarrow{N}_{kp}^{(i)} \overrightarrow{\sigma}_{pq} (\overrightarrow{N}_{ql}^{(i)})^T dV_i}{\sum_{i=1}^N \int_{V_i} \overrightarrow{N}_{kp}^{(i)} \overrightarrow{\sigma}_{pq} (\overrightarrow{N}_{ql}^{(i)})^T dV_i} \quad (\text{Equation 18})$$

where $\overrightarrow{D}_n^{\text{eff}}$, σ_n^{eff} , and d_{nk} respectively represent the effective electric displacement matrix, the effective stress vector of metamaterial and the effective piezoelectric charge constant defined in global 1–2–3 coordinate system, and $k, n, l=1, 2, 3$ should follow the situation. $\overrightarrow{N}^{(i)}$ is the system transformation matrix containing components with respect to the location pattern vector. V_i is the volume of each rod in FMP_x. σ_k is the externally applied stress field in global system, defined by multiplying the stress vector σ_{pq} and matrix $\overrightarrow{N}^{(i)}$, and $p, q=x, y, z$ is the local principal stress in three directions. This allows the displacement generated in the positive pressure direction (1–2–3) applied on FMP_x to be converted to

the local elemental body through $\mathbf{N}^{(i)T}$.

The former experiment demonstrated that the mechanical responses of FMP_x could be uniquely tailored, whether in high or low vertical positive applied pressure. Through alternation of geometric parameters of the unit cell, the density and mechanical behavior under compression could be adjusted. Finite element methods and models of five types of FMP were constructed by CAE simulation (COMSOL), as presented in Figures S9C-S9D. Compared with each result, the compressive strength of FMG was positioned between that of FMP_3 and FMP_2 . Concurrently, at minimal strains, its sensitivity mirrored that of FMP_1 , primarily attributed to the ease of deformation of the individual rod. In direct proportion to the accumulation of local stress, the output voltage of FMP_3 was the highest, and FMG can work at suitable loading.

In the impact load experiments (the snap photoshoot of FMG_3 loading selected in Figure S10), the first-order derivative trend of the mechanical response curve of FMP under compression aligned with that of bulk-type devices and conformed to the theoretically derived $\sigma-\lambda$ curve pattern. FMP_3 , the highest structural density device, was compared as the relative greatest compressive strength and the highest structural rigidity. Responses increased or decreased systematically with changes in structural dimensions. In short, the orderly stacking of the octagonal lattice unit cells can facilitate the programming of piezoelectric FMP.

Polarization process and FMP device response.

In the electric fields, dielectric phenomenon exhibits two primary material response mechanisms: conduction and polarization¹⁹. Polarization is characterized by a shift in the center of positive and negative charges within the dielectric, leading to the generation of an electric dipole moment²⁰. The polarization process of BNNS composite FM, a molecular crystal, can be attributed to thermal motions inherent in spontaneous polarization, electron relaxation polarization stemming from lattice defects, and molecular orientation polarization²¹.

Films or bulk types of 2D FM were encapsulated in a sandwich configuration (as a control group), with indium tin oxide (ITO) conductive glass on one side and Au/Cr electrodes (NSC-3000 Sputter Coater, Nano-Master Inc., Austin, TX, USA) pressed on the other (Figure S11A). A direct current polarization voltage, ranging from 2.5 to 6 V/ μm , was set on the base of variation in film thickness and nanofiller content. The samples were treated at room temperature for 5 hours without any breakdown occurrence. For the sample with 3D scale and a thickness about 1 cm, a corona polarization apparatus was constructed, as depicted in Figure S11B. By insulating oil situated 2 cm below the 3D FMP_x needle tip, two alumina plates with high dielectric properties were placed on either side, to prevent localized discharges between the electrodes. The potential difference between the needle tip and the bottom copper plate was set to 10 to 20 kV depending on the sample height. FMP_x and FMG were continuously treated for 2 hours using a DC polarization voltage of 1.25 kV/ μm (Figure S11C), connected and verified by a ferroelectric measuring system (Hysteresis Version 3.1.1, Radiant Technologies, Inc., Albuquerque, NM, USA).

The charge responses of FMP_x, FMG, and flat film (control group) devices, comprising a charge collector and a six-axis force sensor, were totally encapsulated. In the initial compression stage at 1 kPa, three characteristic peaks were identified for FMP₁ (Figure S11D). The delay response times were recorded as 6.7 ms, 4.1 ms, and 1.9 ms, respectively. Then, the output charges lagged the force by less than 7 ms, which was consistent with the features of piezoelectric charge pulses. It can be attributed to the interaction between soft materials of the impact head and top surface of FMP_x. As the center of applied force did not align with the gravity center of the received one, force and voltage feedback curve showed a gradually decaying nonlinear variation.

Note S6 Response and reinforcement learning of BASS.

Responses of FMG packaged for BASS.

FMG-T/J was adhered to the tip of the robotic finger and at each articulation point based on its surface shape (Figure S12A). FMG-T was encapsulated at the DIP fingertip equipped with a curved electrode, while FMG-J was mounted at the PIP, MCP, and base joint locations. In response to simulated pressures (Figure S12B), sensitivity of FMG-T was linearly fitted to be 30.12 V/MPa. When the tip was subjected to a minor load of 0.5 kPa, the peak voltage reached 724 mV. Under a larger load of 97 kPa, the metamaterial experienced compression saturation with a peak response of 2.39 V. Similarly, the linearity of FMG-T and FMG was evaluated under various load segments, as shown in Note Table S1.

Note Table S1. Comparison of FMG and FMG-T responses

	Light load, V/MPa	Medium load, V/MPa	Heavy load, V/MPa
FMG-T	30.12	12.35	0.04, disability in 97 kPa
FMG	38.81	13.80	1.48, disability in 134 kPa

In terms of stability, FMG-T was tested for 10^4 cycles under a low-frequency (1 Hz) variable load applied by a fatigue measurement exciter (HBK Company, Model Type 4824). Each peak-to-peak voltage of FMG-T remained stable in response. After averaging the force–voltage coupling over multi-cycles, the maximum error in the slope was 1.4%, which falls within the acceptable range (Figure S12C).

Correspondingly, four types of FMG-J at various joint locations were quantitatively acquired charges change in relation to the corresponding bending angles (Figure S12D). When the bending angle was increased to 60°, the response voltage of the metamaterial remained around 80 mV, without significant changes. However, due to the increased bending time, the response time was extended to 459 ms. Furthermore, to quantitatively characterize the rotation angle and voltage, response times were recorded during bending from 0° to 90°. The dotted line of Figure S12E indicated a closely matched and high-level timing of the joint motor. Compared to DIP, MCP had a slower rotation speed and a lower angular velocity with much longer response time.

From an extreme perspective, when the bending speed approached to zero, the response was about

zero. When the rotation speed was infinitely high, it was equivalent to being subjected to an external impact load, with the response peak being the maximum. As illustrated in Figure S12F, bending action was decomposed into acceleration, uniform speed, and deceleration phases. A similar trend was also observed in the response of each FMG–J, which indicated that the amplitude was primarily influenced by the rotation speed.

Features of FMG packaged for robot finger monitoring.

In terms of contact response performance at the tip, there were differences in the signal envelope of the piezoelectric response generated by FMG–T when in contact with objects of three distinct stiffness levels (Figure S13A). When the contact speed was kept constant, the harder the object, the shorter the time taken to reach peak response. However, it was unrelated to the peak value of the voltage. The peak voltage of each small section of the motor was extracted and smoothed into an envelope, from which an approximation of the rising slope from the initial contact to the peak response could be derived. Here, the slope for the soft object (cloth doll) was 0.41, while the slope for the hard object (iron) was 4.5. The hardness of the orange (0.72) fell between these two values. Based on the distinct envelope curve slopes observed for different objects, calibration against standard hardness values was performed, and slope values were captured as an indicator for the device's ability to discern material rigidity.

When subjected to a consistent normal force of 15 kPa, FMG–T was deformed uniformly along the z-axis. It then moved horizontally across surfaces with varying roughness, from coarse to smooth, as depicted in Figure S13B. On the smooth surface of a glass plate, no significant piezoelectric signal was observed. However, on the coarse surface of the fabric, a consistent peak voltage of about 0.5 V was generated, due to the increased frictional forces between the microstructures and interface. When the applied pressure was increased to 30 kPa and the contact surface was changed to cement, the peak-to-peak voltage increased to 1.2 V.

In scenarios mimicking the sensation of a human hand lifting heavy objects, a stable response was consistently observed from FMG–J under heavy-load tests (Figure S13C). The reason can be attributed to its gradient distribution along the axial direction. Upon the application of an additional pulsating load on top of the existing pressure, the output voltage was inversely proportional to the ambient pressure. By applying randomized time and load, a high peak (deformation) and a subsequent low peak (recovery) were found in the responses of FMG–J. This was attributed to the nonlinear rebound of the soft material after compression.

Array-based packaging and signal acquisition in BASS.

On the robotic hand, FMG–T/J from a single finger was replicated in an array, leading to the development of an array and data acquisition system, BASS (Figure S14A). It was primarily divided into four modules, each responsible for signal collection, signal storage, signal analysis, and signal communication, respectively. A matrix array with a 3×5 digital mapping, was encapsulated and organized for BASS, as shown in Figure S14B. Only one flexion joint was present on the thumb, then FMG–T₅₃ was absent. Functionalities not originally possessed by the robotic hand were augmented by

the integration of BASS, including the capability to sense contact gradient (indicated by the orange data bars) and grasp status (displayed on the blue digital screen). In addition, the potential of five motors was extracted and recorded in the array M₁₄ to M₅₄.

Grasping via BASS and reinforcement learning algorithm.

There are four initiative control steps of rotation motors in the roots of each finger during grabbing objects via BASS (Figure 5B), as listed here:

- 1) No-contact phase: Only the FMG–J responded due to joint flexion.
- 2) Onset of contact: Both FMG–T and FMG–J underwent deformation upon contacting an object, continuing until the responses of all devices within the matrix reached 0. Subsequently, motors on each joint were individually halted (with each joint acting as a control unit). All the devices were compressed enough to their stiffness limit at the current motor speed.
- 3) Compression phase: Motors were continuously set to a high level, driving the joints to keep rotating. FMG–J was compressed under high load. Each joint motor was halted when the response of FMG–J reached zero. Additionally, it was essential to ensure that FMG–T also had no output voltage, indicating that the BAS–enhanced robotic hand had fully grasped the object.
- 4) Grasped phase: No relative displacement existed between FMG–T/J and the object to be grasped. Voltages exceeding 10 mV were not detected in the matrix. Ending signal was sent to the system root, marking the completion of entire grabbing.

The reinforcement learning algorithm was selected and surveyed for processing time–domain signals followed by a prediction processer^{22–24} (Figure S14C), which starts at the motion rotated to move, along with the four steps judgment logics, and repeat different times to tighten the target object, to the end of obtaining raw data with stiffness characteristics.

Strategy of reinforcement learning for stiffness recognition.

The time–domain signals from sensors at each joint were extracted and processed into an initial matrix \mathbf{K} , which served as the environment state representation \mathbf{s} . \mathbf{K} was divided into perceptual network layer, low–density feature layer, and policy network layer (Figure S14D). The perceptual layer outputted hardness values with state transition probabilities \mathbf{P} . Hardness values obtained from tester were used as the reference value S , and compared with the fitted K to construct a 3×5–dimensional vector reward function r . The increase in slope k_{ij} of the envelope of each piezoelectric response signal segment was the focus parameter in every action.

By performing multiple grasps on the same object over a period, the probability distributions of hardness matrices in FMG–T/J matrix could be solved, and the probability of slope changes was also considered as the execution strategy π . After the execution, the expected reward was assigned as the state–action function Q with the temporal difference value TD . After capturing the initial grasp segment of the signal in each capture, the current grasp state s and the action reward r after the next grasp state, s' , could be stored in the dynamic vector group r_{ij} . The detailed algorithm flow is explained in Figure S14E. Q value function was repeatedly updated by using formula (19) until convergence or reaching the

predetermined number of iterations.

$$Q(K, S) = Q(K, S) + \alpha_0 [r_{ij} + \gamma \cdot \max(Q(K', S') - Q(K, S))] \quad (\text{Equation 19})$$

α_0 represents the learning rate ($0 < \alpha \leq 1$), and γ is the discount factor ($0 \leq \gamma \leq 1$) used to measure the importance of the next reward r . When grasping various kinds of fruits, BASS repeatedly penalized deviations from the standard values (greater than 500 times) and adjusted the convergence range of the data. The maximum deviation between the standard values and the optimized values was 1.43%, meeting the requirements for a soft-hard perceptible bionic hand (Figure S14F). Through iterative learning, this calculated algorithm successfully attained the optimal perceptual outcomes for hardness values in diverse grasp types and across multiple hardness ranges (Figure S15A and Video S6).

Plotting data on a polar coordinate graph, comparing it with human hands (both the most complete and idealized version) and regular mechanical hands, it was evidenced the grasping times of BASS were falling between the status of fully and no feedback (Figure S15B). Therefore, BASS had the ability to grasp flexible objects (Figure 5C), such as tofu (low modulus, approximating the lattice unit), potato chips (very brittle), and eggs (fragile).

SUPPLEMENTAL FIGURES.

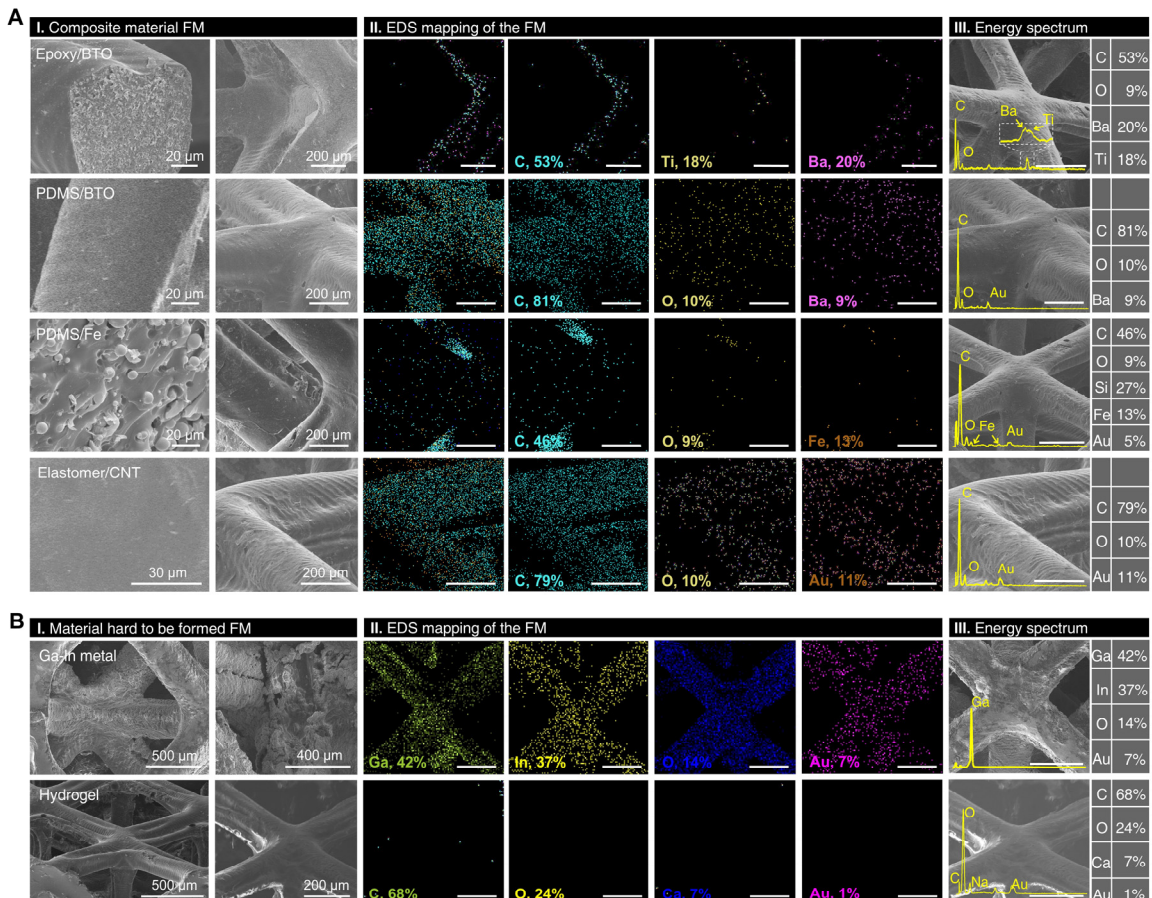


Figure S1. Characteristics of multiple 3D FMs. (A) SEM images, EDS mappings and energy spectra of four conventional composite materials. Contents of each constituent element are quantified on the energy spectrum images through surface scanning. **(B)** SEM images, EDS mappings and energy spectra of three hard-to-be formed FMs.

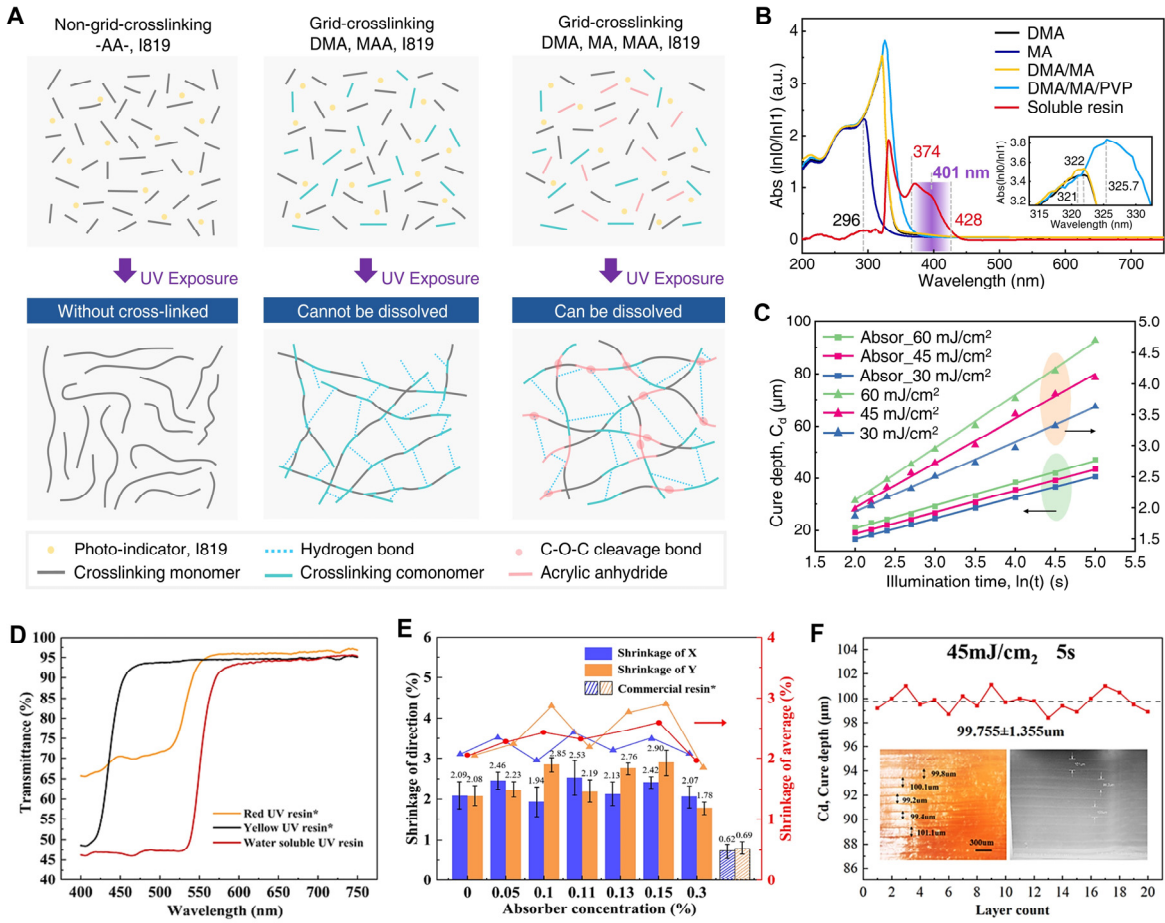


Figure S2. Principle of 3DP soluble resin. **(A)** Schematic diagram of the curing and dissolution mechanism under UV light irradiation about uncross-linked, insoluble and soluble resin, respectively. **(B)** Absorption spectra of various monomers from 200 nm to 750 nm. Illustration data depicted in a zoomed-in spectrum magnified from 310 nm to 330 nm. **(C)** Relative effects of the logarithmic relationship between exposure depth, C_d , and explosion time, t , with three exposure intensities and three absorber compositions. **(D)** Transmittance testing of the soluble resin compared with the commercial resins. **(E)** Shrinkages in two directions of absorber concentration from 0 to 0.3%. **(F)** Stability testing of continuously printing in 20 layers of soluble resin.

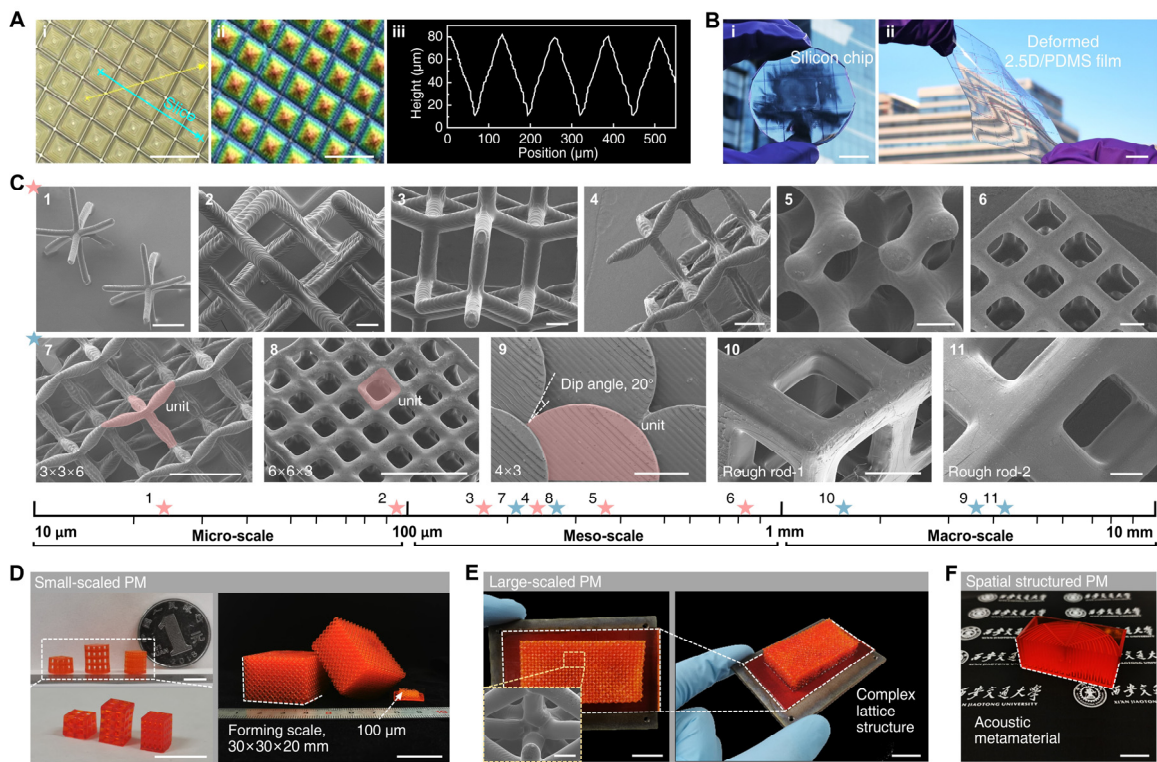


Figure S3. Cross-scaled forming capability of PM. **(A)** Results of Fourier transform infrared spectroscopy (FTIR) and laser scanning confocal microscope for 2.5D microstructure formed in PDMS film. (i) Optical microscope image. (ii) Microstructure height map generated by the vision algorithm. (iii) Height curves of the yellow section in image (i) followed by the change in section position. **(B)** (i) Image of 2.5D pyramidata microstructural coated in a silicon chip. (ii) Image of the tensile state of PDMS film. **(C)** Various formed 3D PMs with cross-scale resolution from 22 μm to 4.2 mm, containing (1) octagonal truss, (2) space truss, (3) four-corner truss, (4) pentamode units, (5) minimum surface units, (6) cubic units, (7) pentamode lattice, (8) cubic lattice, (9) fish scale like lattice, two cubic lattices with rough scale rods of (10) and (11). **(D)** Small scale PMs with feature resolution of 100 μm , 350 μm and 500 μm , scale bars: 1 cm. **(E)** Large scale octagonal units composed PM, scale bars: 1 cm. **(F)** PM made for the acoustic metamaterial with the minimum resolution of 2 mm, scale bar: 2 cm.

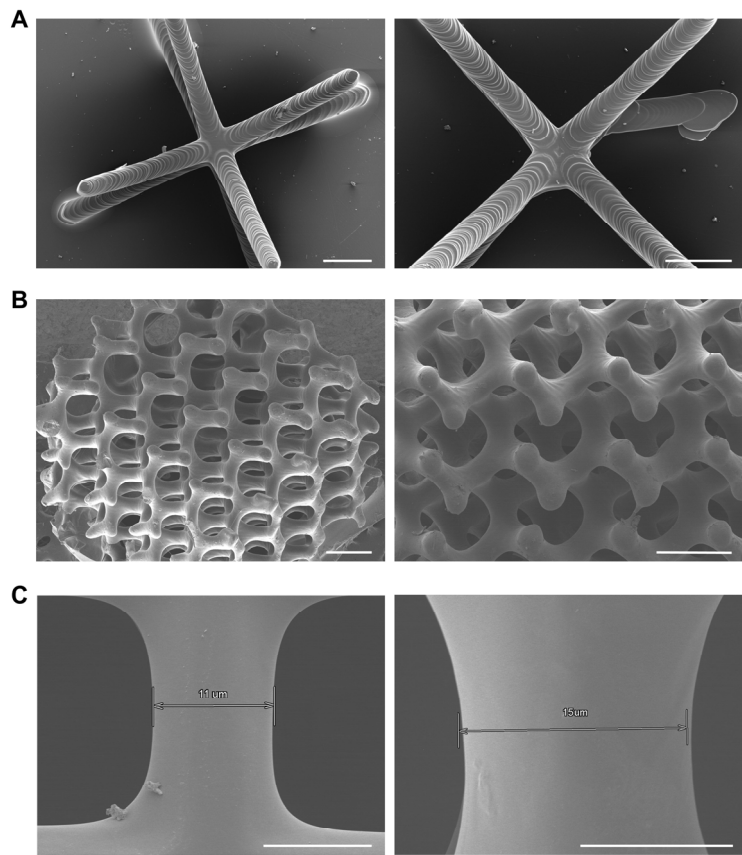


Figure S4. Three printing samples to achieve extreme features. (A), Octagonal truss sample with a structural aspect ratio of 5 (i) and 20 (ii); scale bars: 20 μm . (B), Minimum surfaces crystal truss to show the printing complexity in micro-scale; scale bars: 100 μm . (C) Two samples to validate the minimum printing size to 11 μm (i) and 15 μm (ii), respectively; scale bars: 10 μm .

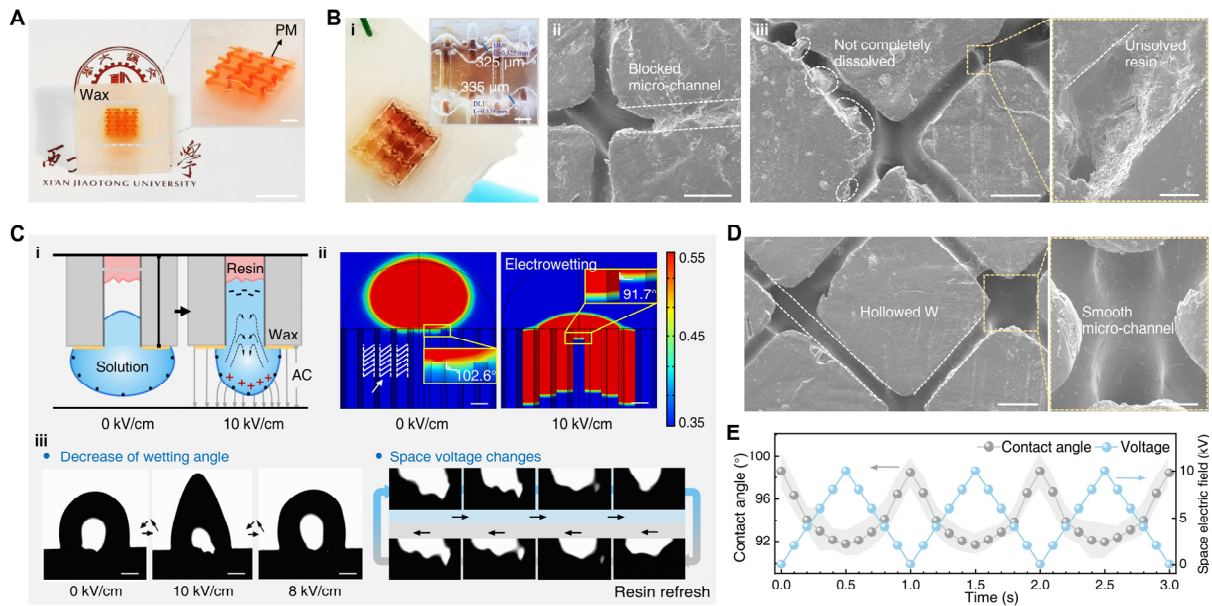


Figure S5. Simulation and experiments of PM dissolution. **(A)** Wax coated 3D PM. **(B)** (i) Experiment image of incomplete dissolution with residual PM. (ii) SEM image of the blockage PMs in micropores, scale bar: 500 μm . (iii) SEM image of PMs which are not completely dissolved and stuck on surfaces, scale bar: 500 μm . **(C)** (i) Schematic diagram of the infiltration state of superhydrophobic panel. (ii) Simulation of the droplet electrowetting in an ideal model. (iii) Optical images of liquid dissolution droplets with different DC electric fields (left), video silhouettes of micropore repeated infiltration with sawtooth-shaped voltage (right). **(D)** SEM image of the hollowed W and the smooth inner panel wall, scale bars: 500 μm . **(E)** Jagged voltage fluctuation cycled from 0 to 10 KV, and the average value of CA caused by electrowetting.

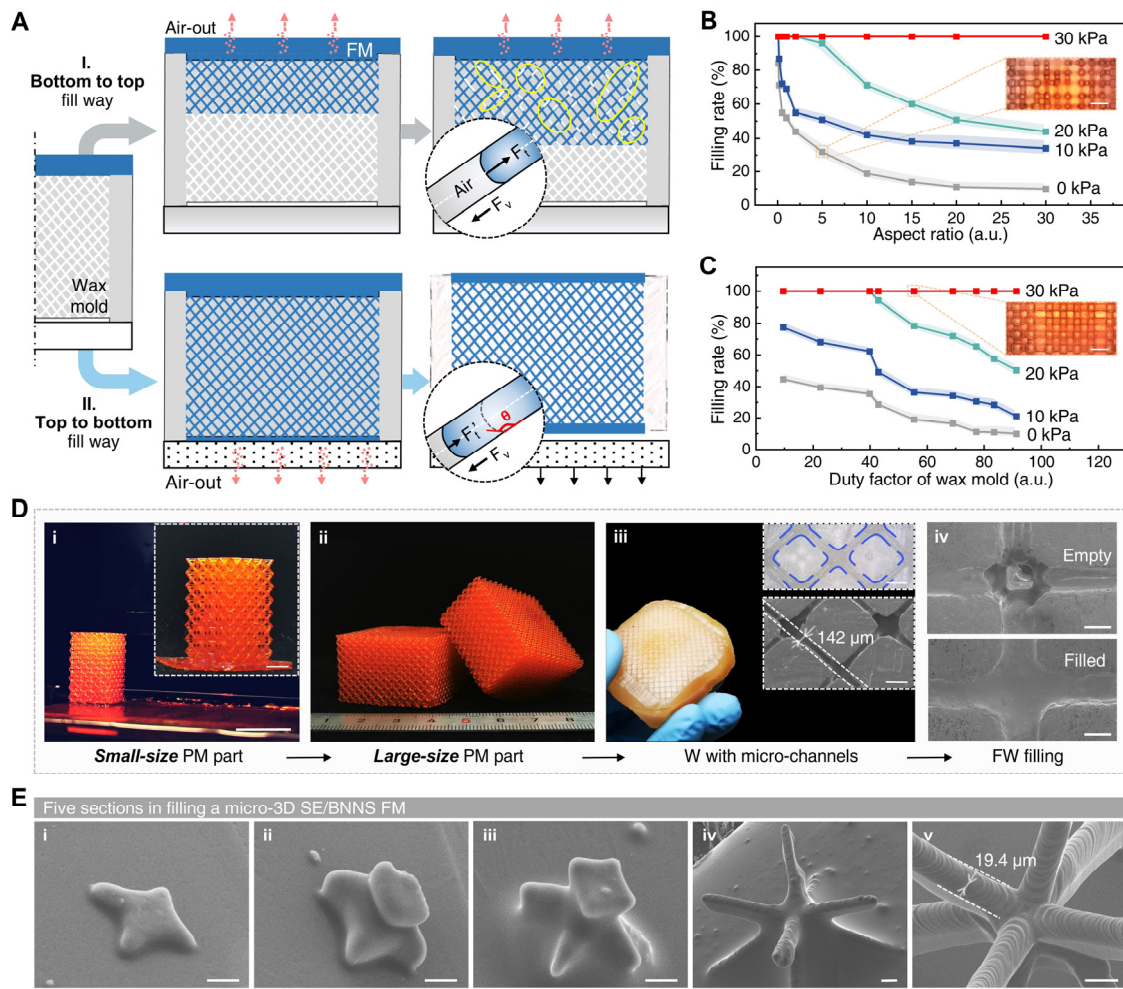


Figure S6. Processes and results of continuous filling. (A) Schematic diagram of two filling strategies, bottom-to-top filling and top-to-bottom filling, reflected two directions of liquid accomplished by air squeezed and discharged. (B) Filling rates of the W with different aspects from 0 to 30 and relative pressures in 0, 10, 20, and 30 kPa, insert is the failed filling sample within air bubble appeared continuously. (C) Values of filling rates under various duty factors (0 to 90) in W with pressures (0, 10, 20 and 30 kPa), insert is the successfully filling in W. (D) Process of a fully filled composite mold templated from a small (i) and large size PM (ii). (iii) Photographs of the hollowed W inserts are the optical and SEM images of W, scale bar: 500 μm . (iv) SEM images of the hollowed W and W filled with FM, scale bars: 200 μm . (E) Five inner sections in filling a micro-3D BNNS reinforced silicon elastomer matrix FM, shown as the feature of minimum resolution nearly 20 μm .

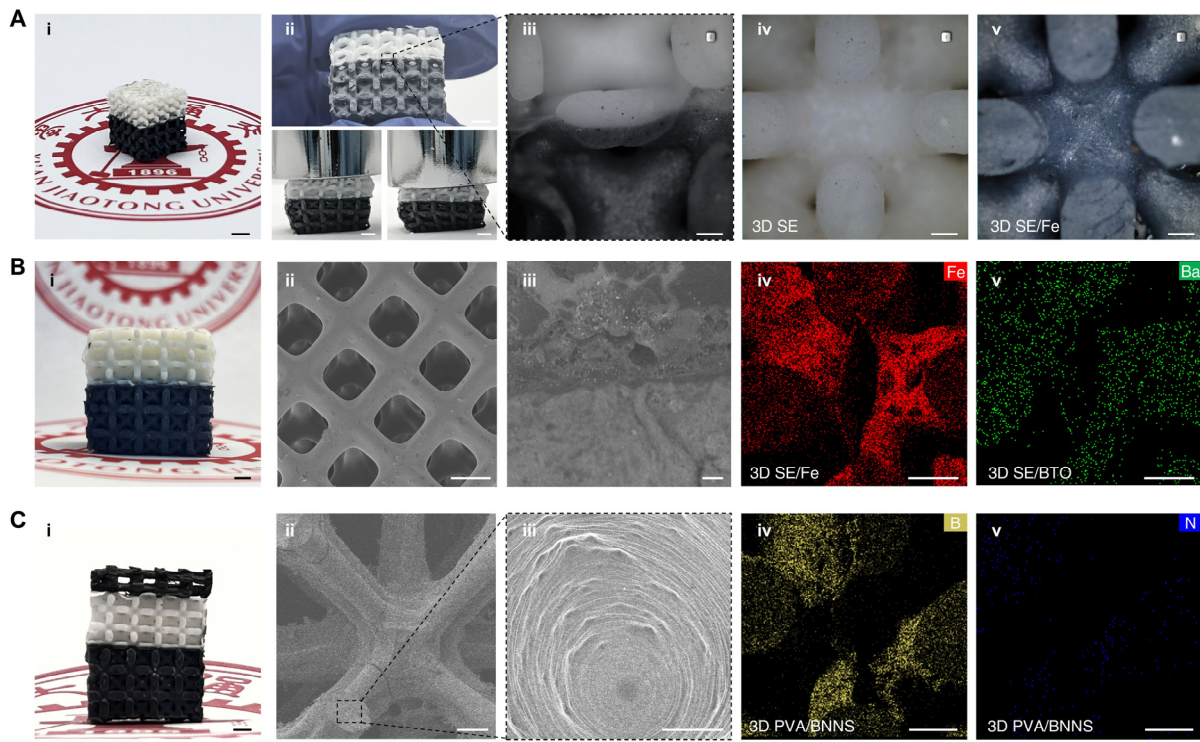


Figure S7. Multi-material deposition 3D FM. **(A)** Optical images of a 3D FM formed by SE and SE/Fe; scale bars: 1 mm (i-ii) and 100 μ m (iii-v). **(B)** Optical image of a 3D FM with SE/Fe composite combined with SE/BTO composite (i); scale bar: 1 mm. (ii) SEM image of 3D SE/Fe lattices; scale bar: 500 μ m. (iii) SEM image of the section of the interface of two FM; scale bar: 50 μ m; (iv-v) EDS mapping of the elements Fe and Ba in each part, respectively. **(C)** (i) Optical image of a sandwiched 3D FM consisting of PVA/BNNS/CNT aerogel, SE/Fe, and SE/BNNS; scale bar: 1 mm. (ii-iii) SEM images of the 3D aerogel; scale bars: 500 μ m (ii) and 50 μ m (iii). (iv-v) EDS mapping of the elements B and N in 3D PVA/BNNS aerogel.

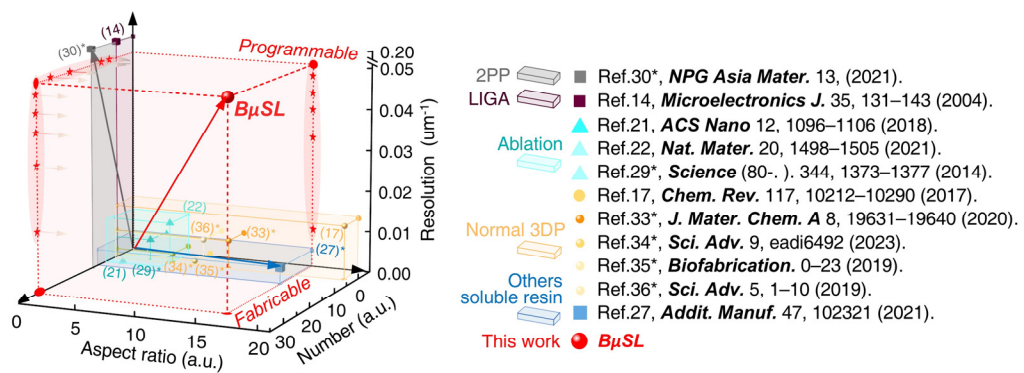


Figure S8. Comparison diagram of micro-3D forming methods. The figure (left) is compared to the minimum resolution, maximum aspect ratio, and FM number that can be printed. The references listed on the right are selected from Tables S2 and S3. The references with * are listed in the main article.

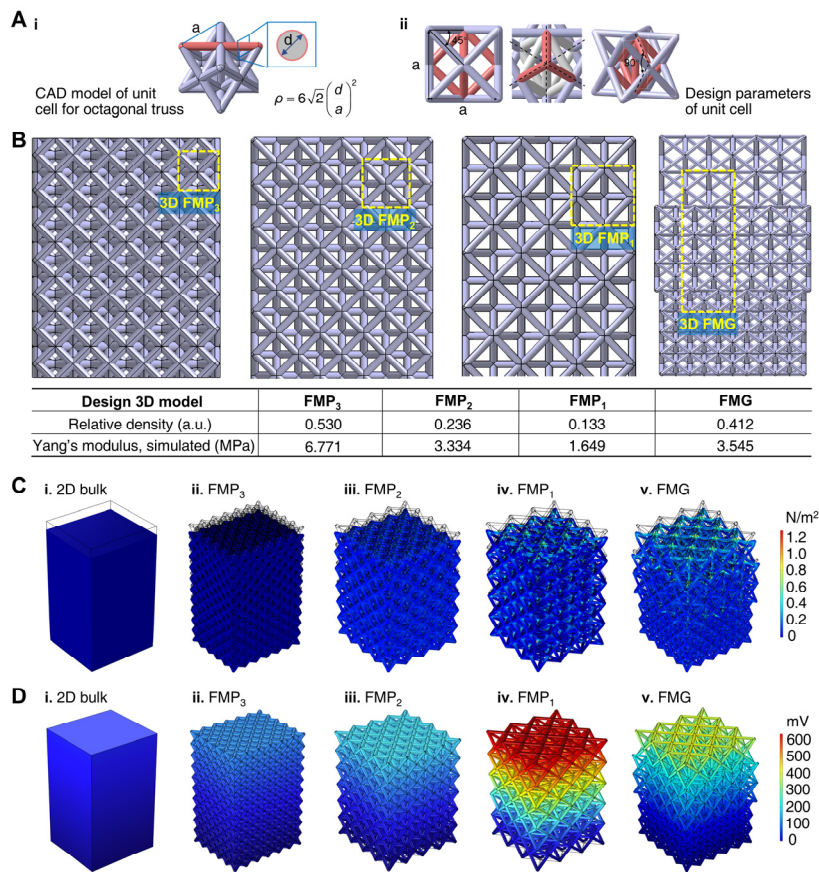


Figure S9. Design models and FEA of 3D FMP_x. (A) CAD model and design parameters of FMP_x. (B) CAD model of 3D FMP₁, FMP₂, FMP₃, and FMG. The table lists the relative density and Yong's modulus simulated in ABAQUS. (C) Mechanical simulations of 2D bulk device (i), 3D FMP_x (ii–iv) and 3D FMG (v) applied with 2 kPa, scale bar: 2 cm. (D) Piezoelectrical simulations of the five devices in positive pressure of 2 kPa, scale bar: 2 cm.

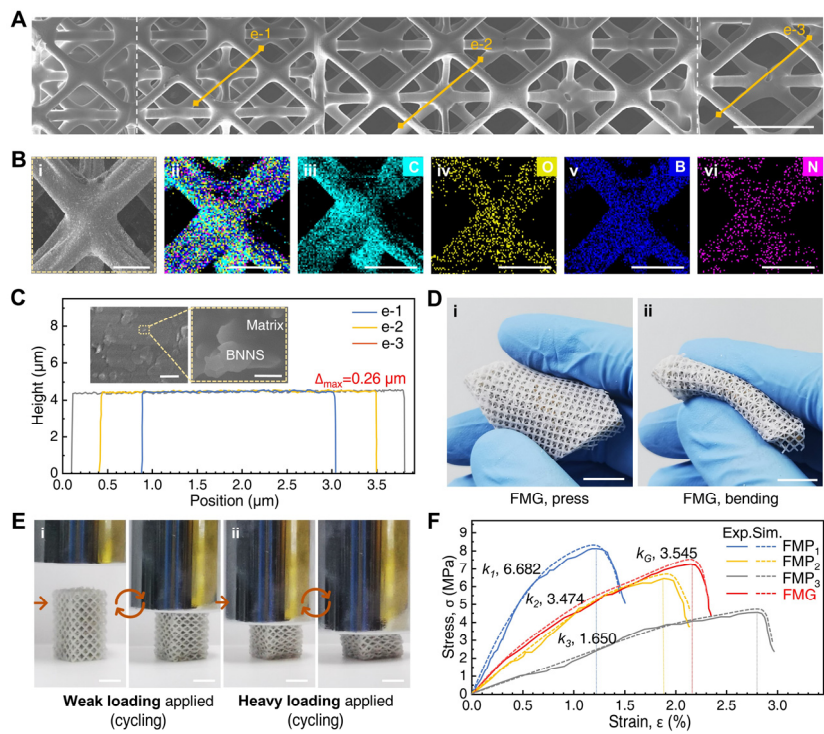


Figure S10. Fabrication and compression texturing of 3D FMG. (A) SEM image of the front view of FMG, scale bar: 1 cm. (B) (i) SEM image of a selected octet unit. EDS mappings of the four main elements of C, O, B, and N, are shown from (ii) to (vi). (C) Surface heights of the microrods composed of three lattices measured by tipping mode of atomic force microscope (AFM). Inset SEM images show the BNNS embedding uniformity in matrix, scale bars: 10 μm, and 500 nm (zoomed-in). (D) Photograph of a large-size 3D FMG during pressing (i) and bending (ii), scale bars: 1 cm. (E) Photographs of compression experiments of FMP₃ applied in light loading cycling (i), and heavy loading cycling (ii); scale bars: 5 mm. (F) Stress–strain curves of FMP₁, FMP₂, FMP₃, and FMG from theoretical simulation and experiments.

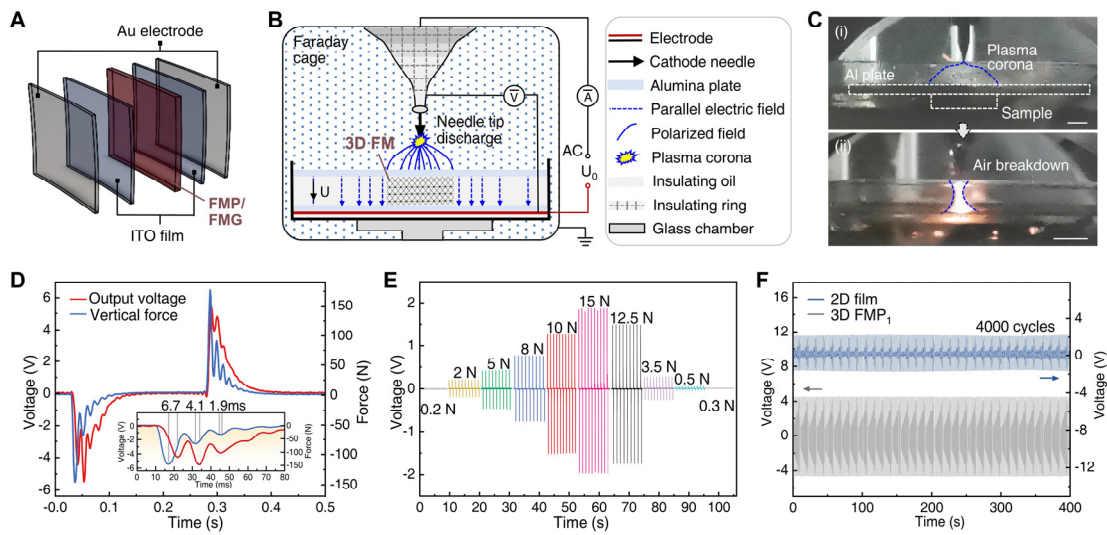


Figure S11. Polarization and dielectric measurement of 3D FMP. **(A)** Schematic diagram of the package of FMP_x. **(B)** Schematic chart of corona polarization instrument. Sample to be polarized is below on a needle tip for uniform plasma field and infiltrated in insulating oil. **(C)** Position of FMP_x under Al₂O₃ plate with a normal plasma corona in graph (i), and a failed treatment with obvious high-voltage air breakdown in graph (ii), scale bars: 2 cm. **(D)** Charge generation transferred for voltage curves followed by the corresponding input impact in a former single time. Insert shows the zoomed-in curves estimating the millisecond time magnitude. **(E)** Step-like electromechanical properties of 3D FMP₁ in which each force segment is stabilized for 10 s. **(F)** Stability responses of 2D film and 3D FMP₁ under 9 N vertical pressure.

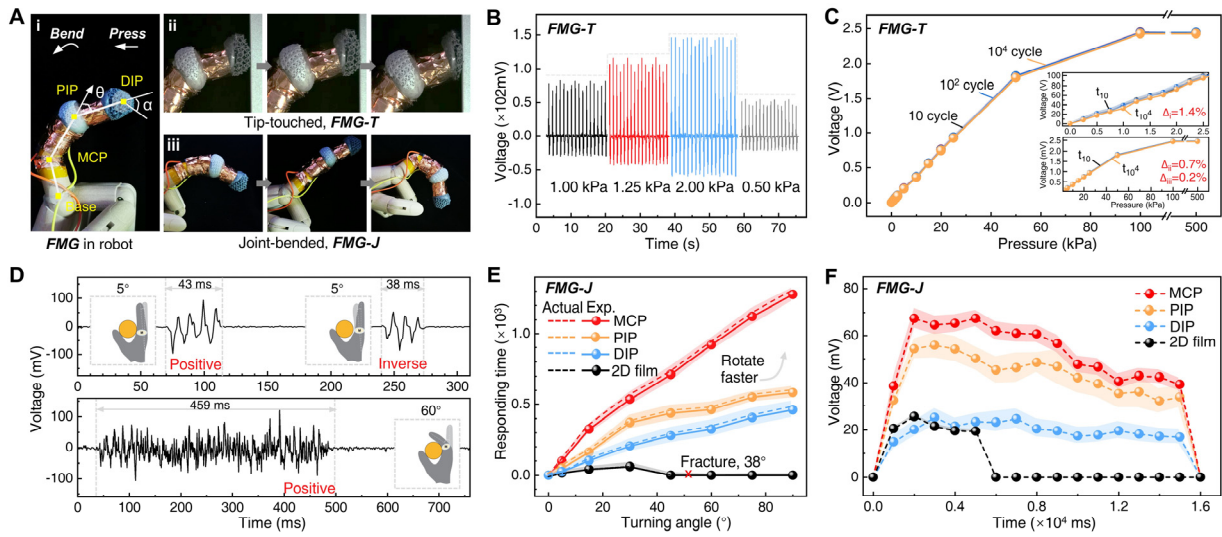


Figure S12. Piezoelectrical responses and stability of FMG-T/J. **(A)** (i) Device installation location of FMG-J/T in index finger, consisting of DIP, PIP, MCP and Base, (ii) compression of fingertip (iii) bending of finger joint. Scale bars: 1 cm. **(B)** Step-like electromechanical properties of FMG-T, pressure applied from 0.5 to 2.0 kPa. **(C)** Stability verification of piezoelectric responses in different periodic ranges. **(D)** Sensing signals of FMG-J followed by MCP rotations. **(E)** Response time for the different turning angles of the FMG-J packaged on three joints. **(F)** Peak-to-peak voltages of the various rotation times recorded by FMG-J.

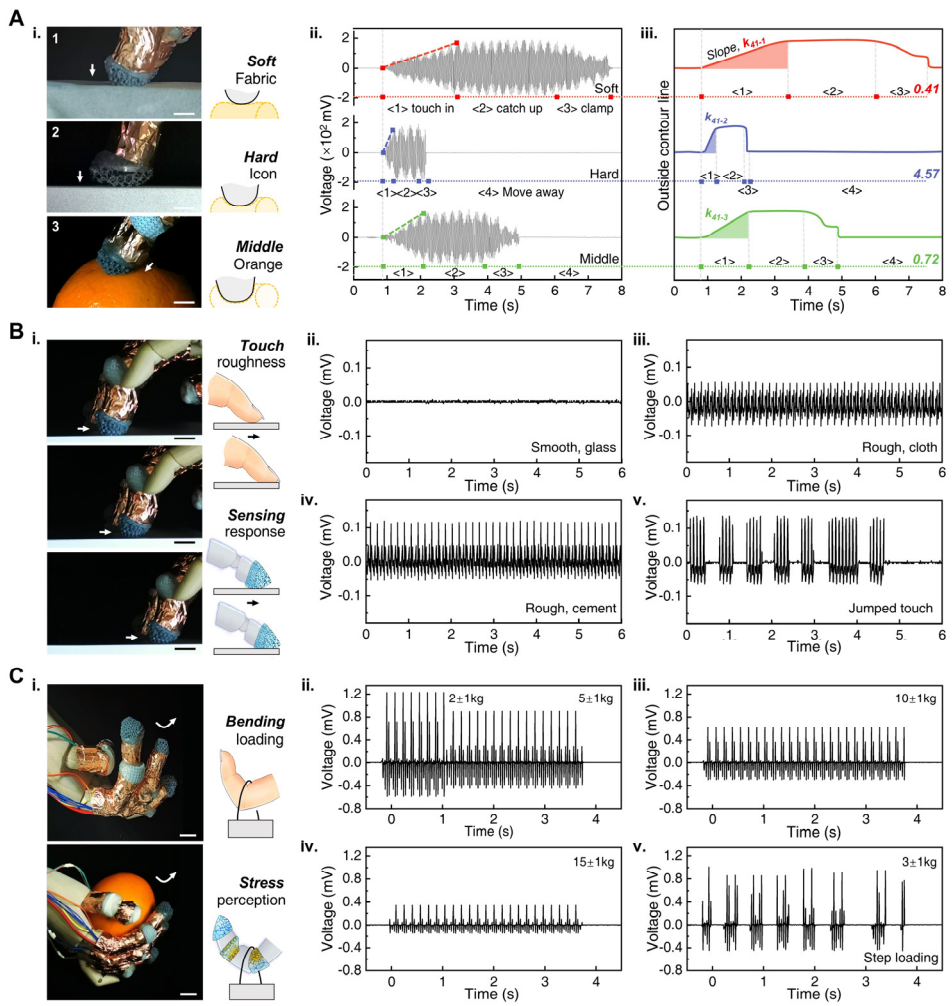


Figure S13. Output features in stiffness, friction, and loading of FMG-T/J. (A) (i) Schematic diagram of touch and pressed sensing for soft, hard, and middle stiffness objects by FMG-T. (ii) Sensing signals of FMG-T response in touch-in, catch-up, clamp and move away phases. (iii) Outside contour line after taking the highest point of the voltage signal corresponding to (ii). (B) (i) Schematic diagram of the friction responses of FMG-T on three surfaces with a constant positive pressure. Responses of moving on smooth glass, rough cloth and rough cement are recorded in (ii), (iii), (iv), respectively. (v) is the jumped touch in a cement surface, which were all tested under 1 kPa. (C) (i) Schematic diagram of FMG-J sensing under a primary loading. (ii–iv) Responses during four pulse loadings. (v) Voltages in eight uniform step pulse loadings with 3 kg base loading.

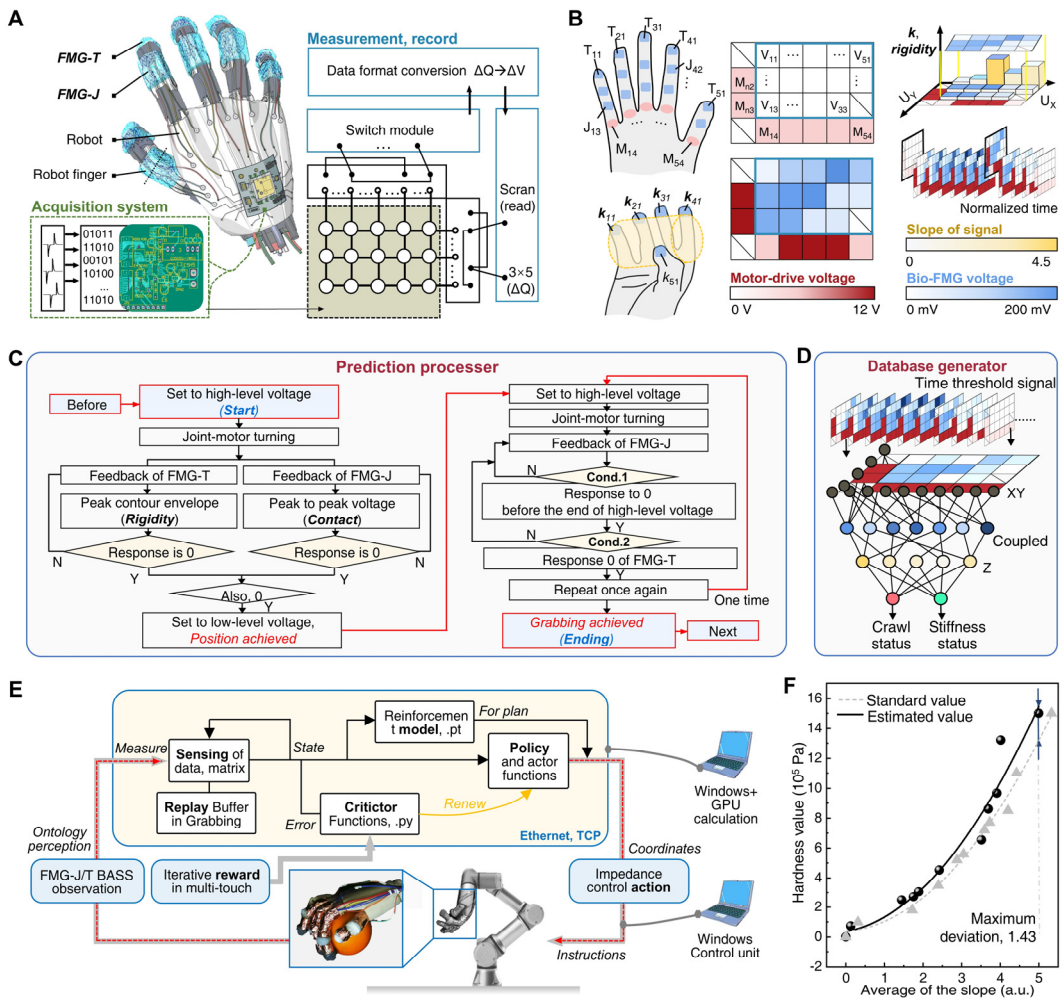


Figure S14. Signal acquisition and training logic of BASS. (A) Schematic diagram of the BASS enhanced robot grabbing, consisting of arrayed sensing, acquisition and measurement modules. (B) (i) Schematic diagram of BASS with a simplified math logic signal matrix. (ii) Visual mapping of signals. (iii) Time normalized slide with a stiffness column chart based on original signal slopes. (C) Mathematics logic and processer of the stiffness prediction algorithm. (D) Data generation model of the piezoelectric voltage, slope value and decoupled steps. (E) Reinforcement learning framework. (F) Hardness comparison of standard and estimated values covering various slopes of fruits.

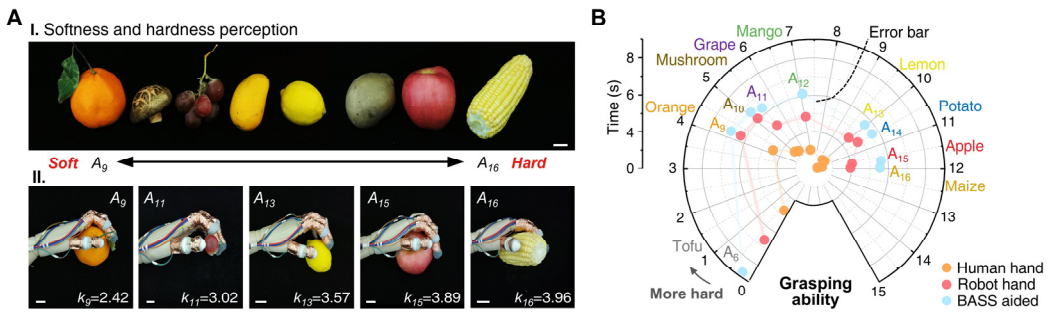


Figure S15. Grabbing different rigidity fruits via BASS. **(A)** (i) Photograph of eight common fruits with different rigidity from soft to hard, marked as A_9 to A_{16} , (ii) Photograph of five typical fruits including tangerine, grape, lemon, apple, and maize, marked with each slope measured in BASS. **(B)** Grabbing time of nine fruits recorded 50 times compared to the grasping ability of the human hand, robot hand, and BASS–assisted robot hand.

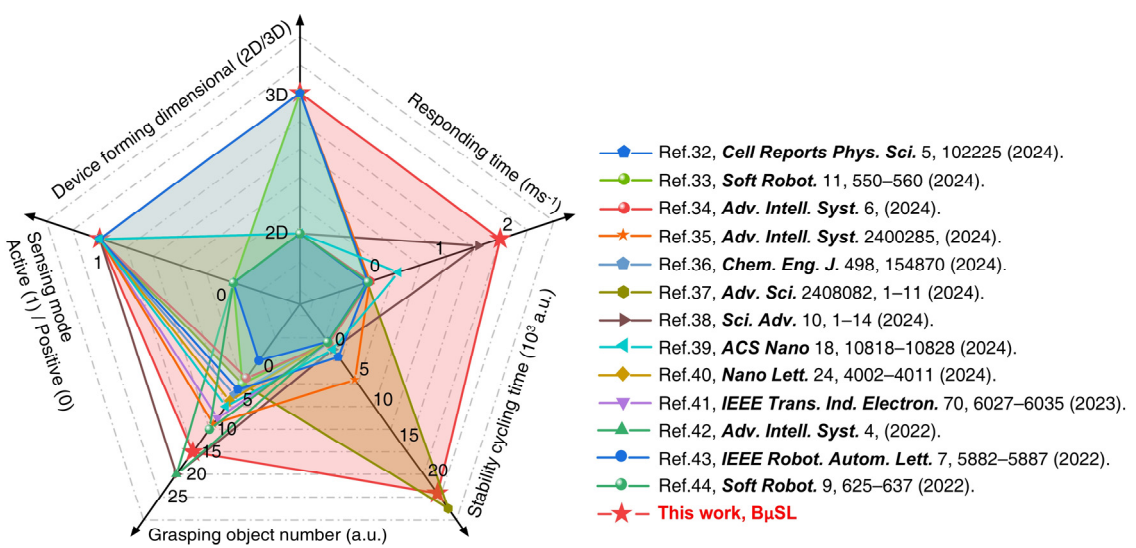


Figure S16. Comprehensive performance comparison of the typical soft fingers reported in the literature.

SUPPLEMENTAL TABLES.

Table S1. Forming capabilities of the other removable materials compared in Figure 2H.

Forming strategy	Type of 3DP	Minimum feature size	Maximum aspect ratio	Removable material kind	Dissolution temperature	Ref.
3D template assisted	Other soluble resin	2 mm	≤ 0.5	DIBA–MSA–DAA ^a THF ^b	50°C	28 ^{*h}
		1.3 mm	≤ 7	AA–MA NaOH solution ^c	R.T. [*]	22 ^{*h}
		1 mm	≤ 5	AA–MA NaOH solution	R.T.	16
		500 µm	≤ 15	AA–MA NaOH solution	R.T.	26 ^{*h}
		500 µm	5	TMAEA–co–NVP ^d DI water	R.T.	27 ^{*h}
		500 µm	5	AA–MA NaOH solution	R.T.	25
		250 µm	3	ACMO–HUA ^e DI water	90°C	24 ^{*h}
		150 µm	10	AA–MA NaOH solution	R.T.	26
		75 µm	40	AA–MA NaOH solution	R.T.	27
	Fused deposition modeling	450 µm	5	ABS resin ^f Acetone	R.T.	25 ^{*h}
Photolithographic transfer	Lithography	1 µm	≤ 20	Photoresist ^g NaOH solution	R.T.	12 ^{*h}
	Nanoimprinting	5 µm	0.06	Photoresist ^g NaOH solution	R.T.	28
3D template assisted	UV curing	50 µm	≤ 30	AA–MA–MAA KOH solution ^c	R.T.	This work

^{*}: Room temperature, 25°C, at standard atmospheric pressure, 101 kPa.

^a: Diisobutyl adipate (DIBA). Methyl N–Succinimidyl Adipate (MSA). Diacetone alcohol (DAA).

^b: Tetrahydrofuran (THF).

^c: Sodium hydroxide (NaOH). Potassium hydroxide (KOH).

^d: N–Methyl–N–(N,N–dimethylaminoethyl)–aminoethanol (TMAEA). N–Vinyl–2–pyrrolidone (NVP).

^e: 4–acryloyl morpholine (ACMO). Hindered urea acrylate (HUA).

^f: Acrylonitrile Butadiene Styrene (ABS).

^g: The kind of photoresist is 8–group epoxy–based negative photoresist, SU–8.

^h: The reference is listed in the main article.

Table S2. Other 3DP methods for multiple 3D metamaterials.

Forming strategy	Type of 3DP	Functional material	Precision	Maximum aspect ratio	Removal process	Ref.
				Forming type		
Ablation	UV curing	Graphene	200 µm, 3D truss	3	Muffle furnace	²⁹ (Fig. 3D)
				1		
		Carbon	5 µm, 3D micro-lattice	10	Ni coating ablation	³⁰ (Fig. 3D)
				4		
		Ni-Al ₂ O ₃	10 µm, nested 3D truss	12	Ablation	³¹
				4		
2PP	Lithography	Co-Cr-Ni	350 nm, 3D nanolattice	3	–	³²
				1		
LIGA	Lithography	SU-8	5 µm, 3D micro-lattice	5	–	³³ (Fig. 3D)
				1		
Normal 3DP	Polyjet	Commercial resin	10 µm	6	–	³⁴ (Fig. 3D)
				20		
	UV curing	PEDOT: PSS	2 µm, 2.5D elastic circuits	<2	–	³⁵ (Fig. 3D)
				1		
	Electro spinning	TPU-Mxene	2.5D, wrinkled film	<0.1	–	³⁶ (Fig. 3D)
				1		
	UV curing	TPU-CNTs	75 µm, 3D truss	15	–	³⁷ (Fig. 3D)
				1		
	Semi-solid extrusion	PEG-CNT-Mxene-PB	2.5D, 30 µm filament	<2	–	³⁸
				1		
	Semi-solid extrusion	Sodium alginate/gelatin	150 µm, 3D truss	10	–	³⁹
				1		
Other methods	Ink jetting deposition	EGaIn	1.9 µm, 2.5D circuits in PET	>10	–	⁴⁰
				1		
		MoS ₂ -Ag	20 µm, 2.5D arrays	3	–	⁴¹
	UV curing	Photocurable BTO resin	300 µm, 3D truss	10	–	⁴²
				1		
Other soluble resin	UV curing	Multiple	75 µm, 3D truss	40	D.R.T.	²⁷ (Fig. 3D)
				4		
		in Table S1	–	–		
Other methods	Ni-coated resin scaffold assisted	Graphene	50 µm, 3D hollowed carbon scaffold	≈15	Powder dissolution	⁴³
				1		
				2		
	UV curing	Tailorable UV resin	100 µm, 3D foam	8	–	⁴⁴
				10		
	Laser melting deposition	Ti-Al ₂ O ₃	3 mm, 3D pillar	1.5	–	⁴⁵
				5		
	Ink jetting deposition	Multiple inks	250 µm, 3D truss	12	–	⁴⁶
			–	8		

‘–’means the performance is unverified.

Table S3. Compared features to this approach, B μ SL.

		Functional material	Potential application	Maximum aspect ratio	Removal process	Ref.	
				Forming type			
B μ SL (This work)	UV curing	PDMS	Resistance e-skin	>20	D.R.T.	–	
		PDMS-CNT	Piezoresistive, capacitance		D.R.T.		
		PDMS-Fe	Shielding		D.R.T.		
		PDMS-BTO	Ultrasonic transducer		D.R.T.		
		Epoxy	Toughening		D.R.T.		
		Epoxy-BTO	Piezoelectric, hydrophone		D.R.T.		
		Epoxy-Mxene	Piezoelectric, piezoresistive, Shielding		D.R.T.		
		LCE ⁱ	Thermal actuation		D.R.T.		
		LCE-CNT			D.R.T.		
		LCE-PVDF-CNT			D.R.T.		
		Ga-In	4D printing, e-skin, mechanics design		Dissolved in non-polar solvent ⁱⁱⁱ		
		Hydrogel	Bio-truss engineering, wound repair	>20	D.R.T.	–	
		TPU	e-skin		D.R.T.		
		TPU-CNT	Piezoresistive, Electroencephalogram		D.R.T.		
		TPU-BNNS	Piezoelectric		D.R.T.		
		TPU-BNNS-CNT			D.R.T.		
		Mxene aerogel	Shielding thermal protection, piezoresistive, piezoelectric		Dry and remove in inert gas		
		PVA-BNNS aerogel	Humidity perception		Dry and remove in inert gas		
		SE ⁱⁱ	e-skin		D.R.T.		
		SE CNT	Piezoresistive		D.R.T.		
		SE-PVDF	Piezoelectric		D.R.T.		
		SE-PVDF-BNNS			D.R.T.		
		SE-PVDF-CNT-BNNS			D.R.T.		

ⁱ: LCE is the abbreviation of liquid crystal elastomer.

ⁱⁱ: SE is the abbreviation of silicon elastomer.

ⁱⁱⁱ: The non-polar solvent includes xylenes, ethyl ether, tetrachloromethane, petroleum ether, and so on.

Table S4. Performance comparison of bioinspired soft fingers reported in the literature.

Acquisition of compliance	Sense mode	Yes/No Bimodal perception	Detected sensitivity	Responding time	Stability cycle	Grabbing range	Ref.
Mold casting via various pre-made die	Active	Yes					
		Stiffness, force, and bending	0.02° 0.4 mN	50 ms	>2000	5 fruits from Tofu to tomato, artery location, pulse-taking	47
	Active	No					
		Shape-adaptability, grasping	0.0014 J	80 ms	—	4 objects	48
	Active	Yes					
		Stiffness, force, and bending	0.01 N 106.96 mN / nm	20 ms	250	3 objects for roughness recognition and grasping (0.01 N to 3 N)	49
	Active	Yes					
		Shape-adaptive and tactile sensing	7.49% to 10.36% dB/kPa	20 ms	5000	Fruit and 3 cylindrical objects grasp, posture recognition	50
	Active	No					
		Roughness, grasping	—	20 ms	—	6 objects for roughness recognition	51
Lithography packaged	Active	No					
		Force sensing	0.15 kPa ⁻¹	126.2 ms	22000	24 sensing units within 0-100 kPa	52
	Active	Yes					
		Texture recognition, force, grasp	0.52 to 261 mV/N	0.6 ms	10 ³	15 objects for roughness recognition, 8 types for grasp	53
	Active	Yes					
		Force and gestures recognition	0.04 kPa	21 ms	10 ³	Sensing ranges from 5 Pa to 450 kPa	54
	Active	Yes					
		Grasping and object perception	1.69 kPa ⁻¹ 0.58 V/kPa	60 ms	—	6 film cognition and real-time grasping ball	55
3D printing, laser cuts and mold assembly	Active	Yes					
		Tactile perception, grasping	—	20 ms	200	Serious objects grasping	56
	Passive	No					
		Motor actuation	—	20 ms	—	23 objects grasping for gestures	57
	Passive	No					
		Pneumatic actuation	—	>500 ms	5	None grasping	58
	Passive	No					
		Pneumatic actuation	—	>500 ms	50	8 objects grasped with different shapes	59

BμSL for programmable free-assembly soft continuum	Active	Yes	27.4 V/MPa 0.1° 0.1 mN	0.5 ms	10^4	16 objects grasping, functions integration	This work
		Stiffness, force, bending, shape					

‘–’means the performance is unverified.

SUPPLEMENTAL REFERENCES.

1. Nikpour, S., Ansari-Asl, Z., Sedaghat, T., and Hoveizi, E. (2022). Curcumin-loaded Fe-MOF/PDMS porous scaffold: Fabrication, characterization, and biocompatibility assessment. *J. Ind. Eng. Chem.* *110*, 188–197. <https://doi.org/10.1016/j.jiec.2022.02.052>.
2. Liu, F., Alici, G., Zhang, B., Beirne, S., and Li, W. (2015). Fabrication and characterization of a magnetic micro-actuator based on deformable Fe-doped PDMS artificial cilium using 3D printing. *Smart Mater. Struct.* *24*, 35015. <https://doi.org/10.1088/0964-1726/24/3/035015>.
3. Pei, X., Liu, G., Shi, H., Yu, R., Wang, S., Liu, S., Min, C., Song, J., Shao, R., and Xu, Z. (2023). Directional electromagnetic interference shielding of asymmetric structure based on dual-needle 3D printing. *Compos. Sci. Technol.* *233*, 109909. <https://doi.org/10.1016/j.compscitech.2023.109909>.
4. Kim, K., Zhu, W., Qu, X., Aaronson, C., McCall, W.R., Chen, S., and Sirbuly, D.J. (2014). 3D optical printing of piezoelectric nanoparticle-polymer composite materials. *ACS Nano* *8*, 9799–9806. <https://doi.org/10.1021/nn503268f>.
5. Cheng, J., Chen, Y., Wu, J.W., Ji, X.R., and Wu, S.H. (2019). 3d printing of BaTiO₃ piezoelectric ceramics for a focused ultrasonic array. *Sensors (Switzerland)* *19*. <https://doi.org/10.3390/s19194078>.
6. Liu, K., Zhou, C., Hu, J., Zhang, S., Zhang, Q., Sun, C., Shi, Y., Sun, H., Yin, C., Zhang, Y., et al. (2021). Fabrication of barium titanate ceramics via digital light processing 3D printing by using high refractive index monomer. *J. Eur. Ceram. Soc.* *41*, 5909–5917. <https://doi.org/10.1016/j.jeurceramsoc.2021.04.044>.
7. Gao, Y., Li, H., and Liu, J. (2012). Direct Writing of Flexible Electronics through Room Temperature Liquid Metal Ink. *PLoS One* *7*. <https://doi.org/10.1371/journal.pone.0045485>.
8. Taylor, S.L., Shah, R.N., and Dunand, D.C. (2018). Ni-Mn-Ga micro-trusses via sintering of 3D-printed inks containing elemental powders. *Acta Mater.* *143*, 20–29. <https://doi.org/10.1016/j.actamat.2017.10.002>.
9. Zheng, Y., He, Z.Z., Yang, J., and Liu, J. (2014). Personal electronics printing via tapping mode composite liquid metal ink delivery and adhesion mechanism. *Sci. Rep.* *4*, 1–8. <https://doi.org/10.1038/srep04588>.
10. Li, G., Zhang, M., Liu, S., Yuan, M., Wu, J., Yu, M., Teng, L., Xu, Z., Guo, J., Li, G., et al. (2023). Three-dimensional flexible electronics using solidified liquid metal with regulated plasticity. *Nat. Electron.* *6*, 154–163. <https://doi.org/10.1038/s41928-022-00914-8>.
11. Ganguly, K., Dutta, S.D., Randhawa, A., Patel, D.K., Patil, T. V., and Lim, K.T. (2023). Transcriptomic Changes toward Osteogenic Differentiation of Mesenchymal Stem Cells on 3D-Printed GelMA/CNC Hydrogel under Pulsatile Pressure Environment. *Adv. Healthc. Mater.* *12*. <https://doi.org/10.1002/adhm.202202163>.

12. Zhang, X., Zhang, H., Zhang, Y., Huangfu, H., Yang, Y., Qin, Q., Zhang, Y., and Zhou, Y. (2023). 3D printed reduced graphene oxide-GelMA hybrid hydrogel scaffolds for potential neuralized bone regeneration. *J. Mater. Chem. B* 11, 1288–1301.
<https://doi.org/10.1039/d2tb01979e>.
13. Yang, R., Guo, Z., Yu, Z., Du, F., Thyagaraja, V.G.N., Lin, L., Yu, D.R., Xu, P., Armstrong, J.N., Lin, S., et al. (2023). 3D-printed conducting polymer hydrogel-based DC generator for self-powered electromechanical sensing. *Nano Energy* 117, 108857.
<https://doi.org/10.1016/j.nanoen.2023.108857>.
14. Zhang, R., Guo, J., Yang, X., Jiang, X., Zhang, L., Zhou, J., Cao, X., and Duan, B. (2023). Ink Based on the Tunable Swollen Microsphere for a 3D Printing Hydrogel with Broad-Range Mechanical Properties. *ACS Appl. Mater. Interfaces* 15, 15917–15927.
<https://doi.org/10.1021/acsami.2c18569>.
15. Stampfl, J., Wöß, A., Seidler, S., Fouad, H., Pisaipan, A., Schwager, F., and Liska, R. (2004). Water soluble, photocurable resins for rapid prototyping applications. In *Macromolecular Symposia*, pp. 99–107. <https://doi.org/10.1002/masy.200451308>.
16. Zheng, X., Deotte, J., Alonso, M.P., Farquar, G.R., Weisgraber, T.H., Gemberling, S., Lee, H., Fang, N., and Spadaccini, C.M. (2012). Design and optimization of a light-emitting diode projection micro-stereolithography three-dimensional manufacturing system. *Rev. Sci. Instrum.* 83. <https://doi.org/10.1063/1.4769050>.
17. Li, L., Rutlin, M., Abraira, V.E., Cassidy, C., Kus, L., Gong, S., Jankowski, M.P., Luo, W., Heintz, N., Koerber, H.R., et al. (2011). The functional organization of cutaneous low-threshold mechanosensory neurons. *Cell* 147, 1615–1627. <https://doi.org/10.1016/j.cell.2011.11.027>.
18. Yi, Z., Zhang, Y., and Peters, J. (2018). Biomimetic tactile sensors and signal processing with spike trains: A review at Elsevier B.V., <https://doi.org/10.1016/j.sna.2017.09.035>
<https://doi.org/10.1016/j.sna.2017.09.035>.
19. Bodkhe, S., and Ermanni, P. (2019). Challenges in 3D printing of piezoelectric materials. *Multifunct. Mater.* 2, 022001. <https://doi.org/10.1088/2399-7532/ab0c41>.
20. Mahadeva, S.K., Berring, J., Walus, K., and Stoeber, B. (2013). Effect of poling time and grid voltage on phase transition and piezoelectricity of poly (vinylidene fluoride) thin films using corona poling. *J. Phys. D. Appl. Phys.* 46. <https://doi.org/10.1088/0022-3727/46/28/285305>.
21. Ares, P., Cea, T., Holwill, M., Wang, Y.B., Roldán, R., Guinea, F., Andreeva, D. V., Fumagalli, L., Novoselov, K.S., and Woods, C.R. (2020). Piezoelectricity in Monolayer Hexagonal Boron Nitride. *Adv. Mater.* 32, 1905504. <https://doi.org/10.1002/adma.201905504>.
22. Jiménez-Luna, J., Grisoni, F., and Schneider, G. (2020). Drug discovery with explainable artificial intelligence, <https://doi.org/10.1038/s42256-020-00236-4>
<https://doi.org/10.1038/s42256-020-00236-4>.

23. Ibarz, J., Tan, J., Finn, C., Kalakrishnan, M., Pastor, P., and Levine, S. (2021). How to train your robot with deep reinforcement learning: lessons we have learned. *Int. J. Rob. Res.* *40*, 698–721. <https://doi.org/10.1177/0278364920987859>.
24. Harib, M., Chaoui, H., and Miah, S. (2022). Evolution of adaptive learning for nonlinear dynamic systems: a systematic survey. *Intell. Robot.* *2*, 37–71. <https://doi.org/10.20517/ir.2021.19>.
25. Yu, K., Fang, N.X., Huang, G., and Wang, Q. (2018). Magnetoactive Acoustic Metamaterials. *Adv. Mater.* *30*, 1706348. <https://doi.org/10.1002/adma.201706348>.
26. Jiang, Y., and Wang, Q. (2016). Highly-stretchable 3D-architected Mechanical Metamaterials. *Sci. Rep.* *6*, 34147. <https://doi.org/10.1038/srep34147>.
27. Xu, Z., Hensleigh, R., Gerard, N.J., Cui, H., Oudich, M., Chen, W., Jing, Y., and Zheng, X. (Rayne) (2021). Vat photopolymerization of fly-like, complex micro-architectures with dissolvable supports. *Addit. Manuf.* *47*, 102321. <https://doi.org/10.1016/j.addma.2021.102321>.
28. Ko, H., Takei, K., Kapadia, R., Chuang, S., Fang, H., Leu, P.W., Ganapathi, K., Plis, E., Kim, H.S., Chen, S.Y., et al. (2010). Ultrathin compound semiconductor on insulator layers for high-performance nanoscale transistors. *Nature* *468*, 286–289. <https://doi.org/10.1038/nature09541>.
29. Zhang, Q., Zhang, F., Xu, X., Zhou, C., and Lin, D. (2018). Three-Dimensional Printing Hollow Polymer Template-Mediated Graphene Lattices with Tailorable Architectures and Multifunctional Properties. *ACS Nano* *12*, 1096–1106. <https://doi.org/10.1021/acsnano.7b06095>.
30. Ye, J., Liu, L., Oakdale, J., Lefebvre, J., Bhowmick, S., Voisin, T., Roehling, J.D., Smith, W.L., Cerón, M.R., van Ham, J., et al. (2021). Ultra-low-density digitally architected carbon with a struttet tube-in-tube structure. *Nat. Mater.* *20*, 1498–1505. <https://doi.org/10.1038/s41563-021-01125-w>.
31. Zheng, X., Lee, H., Weisgraber, T.H., Shusteff, M., DeOtte, J., Duoss, E.B., Kuntz, J.D., Biener, M.M., Ge, Q., Jackson, J.A., et al. (2014). Ultralight, ultrastiff mechanical metamaterials. *Science* (80-.). *344*, 1373–1377. <https://doi.org/10.1126/science.1252291>.
32. Surjadi, J.U., Feng, X., Fan, R., Lin, W., Li, X., and Lu, Y. (2021). Hollow medium-entropy alloy nanolattices with ultrahigh energy absorption and resilience. *NPG Asia Mater.* *13*. <https://doi.org/10.1038/s41427-021-00306-y>.
33. Malek, C.K., and Saile, V. (2004). Applications of LIGA technology to precision manufacturing of high-aspect-ratio micro-components and -systems: a review. *Microelectronics J.* *35*, 131–143. <https://doi.org/10.1016/j.mejo.2003.10.003>.
34. Ligon, S.C., Liska, R., Stampfl, J., Gurr, M., and Mülhaupt, R. (2017). Polymers for 3D Printing and Customized Additive Manufacturing. *Chem. Rev.* *117*, 10212–10290. <https://doi.org/10.1021/acs.chemrev.7b00074>.

35. Zheng, Y.Q., Liu, Y., Zhong, D., Nikzad, S., Liu, S., Yu, Z., Liu, D., Wu, H.C., Zhu, C., Li, J., et al. (2021). Monolithic optical microlithography of high-density elastic circuits. *Science* (80-.). 373, 88–94. <https://doi.org/10.1126/science.abh3551>.
36. Dong, J., Luo, S., Ning, S., Yang, G., Pan, D., Ji, Y., Feng, Y., Su, F., and Liu, C. (2021). MXene-Coated Wrinkled Fabrics for Stretchable and Multifunctional Electromagnetic Interference Shielding and Electro/Photo-Thermal Conversion Applications. *ACS Appl. Mater. Interfaces* 13, 60478–60488. <https://doi.org/10.1021/acsami.1c19890>.
37. Yin, Y.M., Li, H.Y., Xu, J., Zhang, C., Liang, F., Li, X., Jiang, Y., Cao, J.W., Feng, H.F., Mao, J.N., et al. (2021). Facile Fabrication of Flexible Pressure Sensor with Programmable Lattice Structure. *ACS Appl. Mater. Interfaces* 13, 10388–10396. <https://doi.org/10.1021/acsami.0c21407>.
38. Song, Y., Tay, R.Y., Li, J., Xu, C., Min, J., Shirzaei Sani, E., Kim, G., Heng, W., Kim, I., and Gao, W. (2023). 3D-printed epifluidic electronic skin for machine learning-powered multimodal health surveillance. *Sci. Adv.* 9, eadi6492. <https://doi.org/10.1126/sciadv.adি6492>.
39. Qiongyu Li (2019). Engineering bioprintable alginate/gelatin composite hydrogels with tunable mechanical and cell adhesive properties to modulate tumor spheroid growth kinetics. *Biofabrication* Accept., 0–23.
40. Park, Y.G., An, H.S., Kim, J.Y., and Park, J.U. (2019). High-resolution, reconfigurable printing of liquid metals with three-dimensional structures. *Sci. Adv.* 5, 1–10. <https://doi.org/10.1126/sciadv.aaw2844>.
41. Zeng, M., Du, Y., Jiang, Q., Kempf, N., Wei, C., Bimrose, M. V., Tanvir, A.N.M., Xu, H., Chen, J., Kirsch, D.J., et al. (2023). High-throughput printing of combinatorial materials from aerosols. *Nature* 617, 292–298. <https://doi.org/10.1038/s41586-023-05898-9>.
42. Zeng, Y., Jiang, L., Sun, Y., Yang, Y., Quan, Y., Wei, S., Lu, G., Li, R., Rong, J., Chen, Y., et al. (2020). 3D-Printing Piezoelectric Composite with Honeycomb Structure for Ultrasonic Devices. *Micromachines* 11, 713. <https://doi.org/10.3390/mi11080713>.
43. Chen, Z., Ren, W., Gao, L., Liu, B., Pei, S., and Cheng, H.-M. (2011). Three-dimensional flexible and conductive interconnected graphene networks grown by chemical vapour deposition. *Nat. Mater.* 10, 424–428. <https://doi.org/10.1038/nmat3001>.
44. Chen, D., and Zheng, X. (2018). Multi-material Additive Manufacturing of Metamaterials with Giant, Tailorable Negative Poisson's Ratios. *Sci. Rep.* 8, 1–8. <https://doi.org/10.1038/s41598-018-26980-7>.
45. Zhang, Y., and Bandyopadhyay, A. (2018). Direct fabrication of compositionally graded Ti-Al₂O₃ multi-material structures using Laser Engineered Net Shaping. *Addit. Manuf.* 21, 104–111. <https://doi.org/10.1016/j.addma.2018.03.001>.

46. Skylar-Scott, M.A., Mueller, J., Visser, C.W., and Lewis, J.A. (2019). Voxelated soft matter via multimaterial multinozzle 3D printing. *Nature* *575*, 330–335. <https://doi.org/10.1038/s41586-019-1736-8>.
47. Wang, Y., Wu, H., Li, T., Wang, J., Wei, Z., and Wang, H. (2024). Toward human-like touch sense via a bioinspired soft finger with self-decoupled bending and force sensing. *Cell Reports Phys. Sci.* *5*, 102225. <https://doi.org/10.1016/j.xcrp.2024.102225>.
48. Hou, N., Wu, M., Zhao, Q., Tang, Z., Wang, K., Xu, X., Zheng, X., and Xie, G. (2024). Reticular Origami Soft Robotic Gripper for Shape-Adaptive and Bistable Rapid Grasping. *Soft Robot.* *11*, 550–560. <https://doi.org/10.1089/soro.2023.0051>.
49. Mao, B., Zhou, K., Xiang, Y., Zhang, Y., Yuan, Q., Hao, H., Chen, Y., Liu, H., Wang, X., Wang, X., et al. (2024). A Bioinspired Robotic Finger for Multimodal Tactile Sensing Powered by Fiber Optic Sensors. *Adv. Intell. Syst.* *6*. <https://doi.org/10.1002/aisy.202400175>.
50. Mo, L., Xie, W., Qu, J., Xia, J., Li, Y., Zhang, Y., Ren, T., Yang, Y., Yi, J., Wu, C., et al. (2024). Empowering Particle Jamming Soft Gripper with Tactility via Stretchable Optoelectronic Sensing Skin. *Adv. Intell. Syst.* *2400285*. <https://doi.org/10.1002/aisy.202400285>.
51. Kong, K., Wang, L., Wu, H., Le, Z., Zhang, Y., Wang, Z., Yu, Z., Wu, X., Li, L., Li, W., et al. (2024). Skin-inspired multimodal tactile sensor aiming at smart space extravehicular multi-finger operations. *Chem. Eng. J.* *498*, 154870.
<https://doi.org/https://doi.org/10.1016/j.cej.2024.154870>.
52. Chen, X., Luo, Y., Chen, Y., Li, S., Deng, S., Wang, B., Zhang, Q., Li, X., Li, X., Wang, C., et al. (2024). Biomimetic Contact Behavior Inspired Tactile Sensing Array with Programmable Microdomes Pattern by Scalable and Consistent Fabrication. *Adv. Sci.* *2408082*, 1–11.
<https://doi.org/10.1002/advs.202408082>.
53. Qiu, Y., Wang, F., Zhang, Z., Shi, K., Song, Y., Lu, J., Xu, M., Qian, M., Zhang, W., Wu, J., et al. (2024). Quantitative softness and texture bimodal haptic sensors for robotic clinical feature identification and intelligent picking. *Sci. Adv.* *10*, 1–14. <https://doi.org/10.1126/sciadv.adp0348>.
54. Liu, J., Wang, L., Xu, R., Zhang, X., Zhao, J., Liu, H., Chen, F., Qu, L., and Tian, M. (2024). Underwater Gesture Recognition Meta-Gloves for Marine Immersive Communication. *ACS Nano* *18*, 10818–10828. <https://doi.org/10.1021/acsnano.3c13221>.
55. Zhang, H., Li, H., and Li, Y. (2024). Biomimetic Electronic Skin for Robots Aiming at Superior Dynamic-Static Perception and Material Cognition Based on Triboelectric-Piezoresistive Effects. *Nano Lett.* *24*, 4002–4011. <https://doi.org/10.1021/acs.nanolett.4c00623>.
56. Fang, B., Xia, Z., Sun, F., Yang, Y., Liu, H., and Fang, C. (2023). Soft Magnetic Fingertip With Particle-Jamming Structure for Tactile Perception and Grasping. *IEEE Trans. Ind. Electron.* *70*, 6027–6035. <https://doi.org/10.1109/TIE.2022.3201305>.

57. Zhou, P., Zhang, N., and Gu, G. (2022). A Biomimetic Soft-Rigid Hybrid Finger with Autonomous Lateral Stiffness Enhancement. *Adv. Intell. Syst.* 4.
<https://doi.org/10.1002/aisy.202200170>.
58. Gollob, S.D., Poss, J., Memoli, G., and Roche, E.T. (2022). A Multi-Material, Anthropomorphic Metacarpophalangeal Joint With Abduction and Adduction Actuated by Soft Artificial Muscles. *IEEE Robot. Autom. Lett.* 7, 5882–5887. <https://doi.org/10.1109/LRA.2022.3161714>.
59. Yan, J., Shi, P., Xu, Z., and Zhao, J. (2022). A Wide-Range Stiffness-Tunable Soft Actuator Inspired by Deep-Sea Glass Sponges. *Soft Robot.* 9, 625–637.
<https://doi.org/10.1089/soro.2020.0163>.